ADDIS ABABA UNIVERSITY

ADDIS ABABA INSTITUTE OF TECHNOLOGY

SCHOOL OF MULTIDISCIPLINARY ENGINEERING

CENTER FOR MATERIALS ENGINEERING

MASTER THESIS

A DFT study of 2D Van der Waals Heterostructures of Janus Transition Metal Dichalcogenides with WSe_2 Monolayer for Energy Applications

A Thesis Submitted to Center for Material Engineering in Partial Fulfillment of the Requirements for the Degree of Master of Science

By: Samuel Tilahun Ayele

September 2021

Addis Ababa Ethiopia

Declaration

I, the undersigned, declare that the thesis comprises my work, which has not been submitted and/or approved for the award of a degree by this or any other university and I have fully acknowledged all referred materials used in this thesis work.

Name: Samuel Tilahun

Signature:_____

Submission date: / /2021

ADDIS ABABA UNIVERSITY

ADDIS ABABA INSTITUTE OF TECHNOLOGY

SCHOOL OF MULTIDISCIPLINARY ENGINEERING

CENTER FOR MATERIALS ENGINEERING

MASTER THESIS

A DFT study of 2D Van der Waals Heterostructures of Janus Transition Metal Dichalcogenides with WSe_2 Monolayer for Energy Applications

A Thesis Submitted to Center for Martial Engineering in Partial Fulfillment of the Requirements for the Degree of Master of Science

Approved by the Examining Committee:

Georgies Alene (Ph.D.)		
Advisor	Signature	Date
Tekalign Debela (Ph.D.)		
Co-advisor	Signature	Date
Sintayehu Nibret (Ph.D.)		
Internal Examiner	Signature	Date
Yedilfana Setarge (Ph.D.)		
External Examiner	Signature	Date

Abstract

Atomically thin two-dimensional layered semiconductor materials such as Transition Metal Dichalcogenides (TMDs) have a great potential for solar cells applications due to their favorable photon absorption and electronic transport properties. The combination of 2D materials in the form of van der Waals heterostructures has been proved to be an effective approach for improving the electronic properties of the material. In this work, the electronic properties, such as band structure, bandgap, and band alignment of $MoSSe/WSe_2$, $WSSe/WSe_2$, and $WSeTe/WSe_2$ vdW heterostructures were obtained from Density Functional Theory (DFT). The potential of the exchange and correlation was calculated using the Generalized Gradient-Perdew Berk Ernzed (GGA-PBE) approximation. $MoSSe/WSe_2$, $WSeTe/WSe_2$, and $WSSe/WSe_2$ heterostructures have type-II band alignments, which is advantageous for electron-hole pair separation. Photons can be absorbed directly in $MoSSe/WSe_2$ and $WSeTe/WSe_2$ semiconductors because they have direct bandgaps. $WSSe/WSe_2$ semiconductor has an indirect bandgap, which means that a phonon must also be absorbed or emitted for a photon to be absorbed. The most stable stacking order in heterostructures comprising Janus monolayers of TMDs and WSe_2 has been ascertained based on interlayer binding energies. The binding energies in $MoSSe/WSe_2$, $WSSe/WSe_2$, and $WSeTe/WSe_2$ heterostructures were found to be -18216.75 eV, -38995.69 eV, and -0.3296 eV at an equilibrium interlayer space of 5.75 Å, 4.02 Å, and 4.72 Å respectively, which are more stable than the other tested configurations. The solar cell and photocatalytic applications of the heterostructures were investigated. The structures were not promising for photocatalytic applications because the band levels of semiconductors were insufficient to support full water splitting. When $MoSSe/WSe_2$, $WSSe/WSe_2$, and $WSeTe/WSe_2$ were used as PV materials, the Power Conversion Efficiency (PCE) was found to be 20.16%, 20.48%, and 19.05%, respectively. The results show that it can serve as a suitable photovoltaic material with high efficiency and opening possibilities to develop solar cells based on 2D TMDs materials.

Keywords: JTMDs/WSe_2 Heterostructure, DFT, Bandgap, Band Alignment, and Binding Energy

Acknowledgment

Before anything else, I would like to praise and thank God, the Almighty, for bestowing countless blessings, knowledge, and opportunities that have allowed me to finally complete the thesis.

Foremost, I would like to express my heartfelt gratitude to my advisor Dr. Georgies Alene for the continuous support of my master's thesis, as well as his patience, motivation, and vast knowledge. I consider myself extremely fortunate to have Dr. Georgies Alene as my research advisor. With his support, I was able to take advantage of numerous opportunities to learn how to use new materials and collaborate with others.

Besides my advisor, I would like to thank Dr. Tekalign Debela (Research Professor at Department of Nano and Advanced Materials, College of Engineering, Jeonju University, Republic of Korea) for his persistent support and collaboration.

I offer the deepest gratitude to Mr. Shore Salle (Associate researcher at Ethiopian Space Science and Technology Institute) for his tremendous support and help; also, I would like to thank Ms. Milliyard Likesa for always attempting to keep me on track anytime I encountered difficulties.

Finally, yet importantly, I would like to thank my friends and the entire material engineering staff for their help.

Table of Contents

List of Tables

List of Figures

Abbreviations

2D	Two-Dimensional
TMDs	Transition Metal Dichalcogenides
vdW	Van der Waals
DFT	Density Functional Theory
PV	Photovoltaic
JTMDs	Janus Transition Metal Dichalcogenides
VBM	Valence Band Maximum
CBM	Conduction Band Minimum
SC	Solar Cell
SPSC	Solution Processable Solar Cell
OSC	Organic Solar Cell
DSSC	Dye-Sensitized Solar Cell
QD	Quantum Dot
PSC	Perovskite Solar Cell
PBE	Perdew Berk Ernzed
GGA	Generalized Gradient Approximation
PWscf	Plane-Wave Self-Consistent Field
LDA	Local Density Approximation
ESPRESSO	opEn-Source Package for Research in Electronic Structure, Simulation, and Optimization
VASP	Vienna Ab-initio Simulation Package
BZ	Brillouin Zone
Ry	Rydberg
E	Energy
Å	Angstrom
eV	Electron Volt
E_b	Binding Energy
J_{sc}	Short-Circuit Current Density
V_{oc}	Open-Circuit Voltage

PCE	Power Conversion Efficiency
MD	Molecular Dynamics
SCF	Self-Consistent Field

Chapter 1 Introduction

1.1 Background

Renewable energies are ways to generate energy from unlimited natural resources. These resources are either available with no time limit or replenish more quickly than the rate at which they are consumed. Renewable energies are generally spoken of as opposed to fossil fuel energies. The fossil fuels' stocks are limited and non-renewable in the human timescale. The most known examples of these resources are coal, oil, or natural gas. On the contrary, renewable energies are produced from renewable sources. Renewable energies are also often referred to as "green energies" or "clean energies". Nonetheless, they have a low environmental impact compared to fossil fuels. Several types of renewable energies are produced by different sources such as the sun, wind, or water [1]. It is estimated that in 2017 1.6% of the worldwide-generated energy came from solar sources. At the same time, solar power also contributed to 20% of the total energy growth in this same year [2].

Production of electric current (photovoltaics) and hydrogen from water splitting (photocatalysis) are renewable sources of energy [3]. SCs (also known as "PV ") are used to convert light from the sun, which is composed of particles of energy called "photons", into electricity that can be used to power electrical loads. The SCs are constructed by joining the layers of n-type and p-type semiconductors, where one layer is capable of donating electrons (n-type), and the other layer is capable of accepting electrons (p-type). Since the work reported by Fujishima and Honda in 1972 using rutile titanium dioxide (TiO_2) anode coupled with a platinum cathode for photo-assisted electrolytic water splitting, extensive efforts have been made to construct efficient heterogeneous water splitting systems [4]. The overall water splitting into hydrogen and oxygen gases is achieved since irradiating light on the semiconductor generates electrons (holes) in the conduction (valence) band to reduce (oxidize) water molecules. In addition, one of the most important requirements for a semiconductor, which is suitable for photocatalytic water splitting reactions, is the positions of its band edges.

In particular, recently discovered 2D materials exhibit extraordinary mechanical, chemical, electronic, optical, and magnetic properties that are promising to break through current material limitations in energy applications. The unique characteristics of 2D structures such as high surface-volume ratio, shape, surface charge, anisotropic nature, and tunable functionalities open up their

potential application. 2D materials consistently have exposed crystal lattices compared to other materials, for example, nanowires, nonporous materials, and nanotubes, and thus have superior exposed electrocatalytically active sites at a specific loaded catalyst concentration. Generally, 2D materials are categorized by their structure including graphene, transition metal dichalcogenides (TMDs), layered double hydroxides (LDHs), gC_3N_4, LAPONITE clay, hexagonal boron nitride (h-BN), and black phosphorous (BP) [5]. Among these, TMDs have received considerable interest because of their fascinating properties.

1.2 Two Dimensional Transition Metal Dichalcogenides

Graphene was isolated from highly oriented pyrolytic graphite (HOPG) for the first time in 2004, for which K.S. Novoselov and A.K. Geim were awarded the Nobel Prize in 2010. The linear dispersion at the K points in single-layer graphene's band structure gives rise to novel phenomena, such as the anomalous room-temperature quantum Hall effect, and has opened up a new category of Fermi-Dirac physics [6]. The success of graphene generated explosive interest in other 2D materials, where the use of different elements opens novel opportunities for the exciting new physics and ultimately thin devices [6]. A variety of chemical and physical methods, such as mechanical exfoliation, chemical exfoliation of bulk structures, chemical vapor deposition (CVD) of thin films, and so on, can be used to easily synthesize 2D materials [3], [7]. 2D TMDs, which can be easily exfoliated and present very interesting electrical and optical properties, became one of the most intensely studied areas of solid-state physics and technology [6]. 2D TMDs MX_2 *(M = Mo, W; X = S, Se, Te)* are a large group of layered materials that have gotten a lot of attention because of their intrinsically interesting physical and chemical properties resulting from the multilayer to monolayer structural transition, such as an indirect to direct bandgap transition, large exciton binding energy, and a lot of multi-excitations [8]. Many TMDs form a graphite-like layered structure, resulting in significant anisotropy in their electrical, chemical, mechanical, and thermal characteristics [9]. As shown in Figure 1, TMDs in groups IV-VII are generally layered, but TMDs in groups VIII–X is non-layered configurations [10].

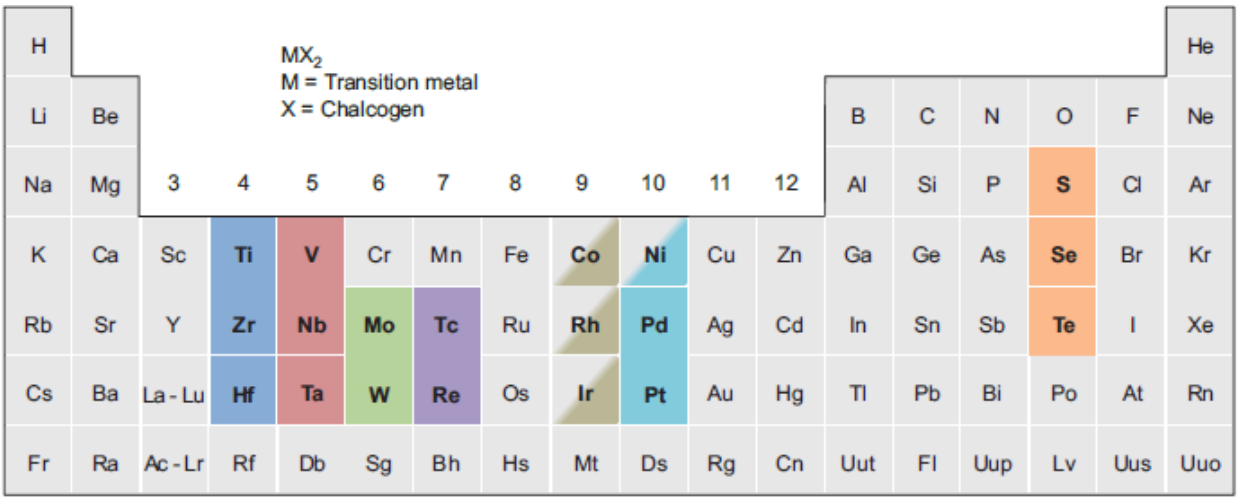

Figure 1. TMDs Compounds with Different Layers [9].

The configuration of 2D monolayer TMDs (MX_2) is a sandwich structure consisting of one transition metal (M) atom layer placed between two chalcogens (X) atom layers, with transition metal atoms (M) such as Mo and W covalently bonded with chalcogen atoms (X) such as S, Se, and Te [11] as shown Figure 2. Each layer in layered formations is generally 6~7 Å atoms thick, with a hexagonally packed layer of metal atoms sandwiched between two layers of chalcogen atoms.

(A) (B)

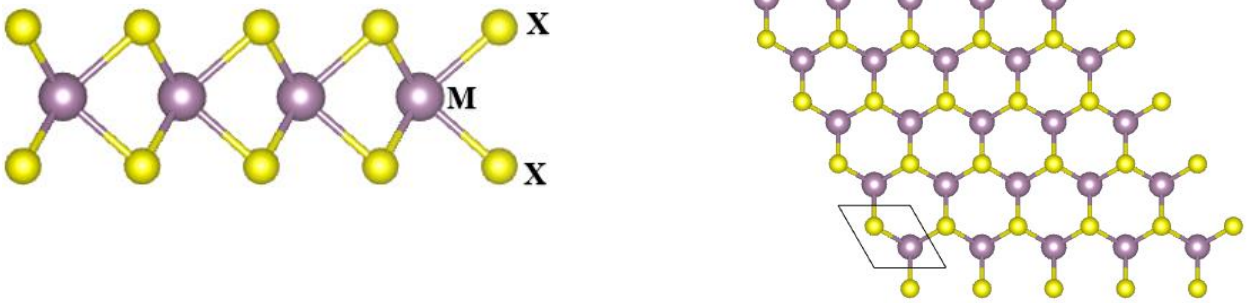

Figure 2. (A) Side and (B) Top Views of TMD Monolayer Atomic Structure (M is Transition Metal and X is Chalcogen).

The interlayer M–X bonds are mainly covalent however, the sandwich layers are connected by weak van der Waals forces, allowing the crystal to break easily along the layer surface [10]. Because the vdW force is several orders of magnitude weaker than in-plane covalent bonding, top-down approaches to obtaining monolayers are viable. The metal atoms contribute four electrons

to the bonding states of TMDs, resulting in metal (M) and chalcogen (X) atoms with oxidation states of +4 and –2, accordingly. The length of the M–M bond varies between 3.15 Å and 4.03 Å depending on the size of the metal and chalcogen ions. These values are 15–25% larger than the bond lengths found in elemental transition metal solids, showing that the d orbitals in TMD compounds have little energy and spatial overlap [10]. Thus, for group IV to group X TMDs, the number of d orbital electrons varies between 0 and 6 [12]. MX_2 2D layered TMDs have outstanding semiconducting characteristics, considerable mechanical flexibility, and are atomically thin. The thicknesses of TMDs are smaller than 1 nm exhibit significant light-matter interactions, allowing for the absorption of incident sunlight of up to 5–10%, which is one order of magnitude greater than that of conventional semiconductors such as GaAs and Si [13]. MX_2 monolayers have direct bandgaps of 1.0-1.9 eV [14], excellent carrier mobility, and a strong spin-orbit coupling (SOC) effect caused by the heavy metal atoms d orbitals [15]. Because of their vast range of applications in catalysis, electrochemical energy storage, photo-catalysis, electronics, optoelectronics, spintronic and photonic nanodevices, 2D materials have gained widespread attention [16].

1.3 Two Dimensional Janus Transition Metal Dichalcogenides

The 2D Janus MXY monolayers can be considered as derivatives of their corresponding TMDs MX_2, which exhibit a high dipole across the plane due to different atomic species on each side of the metal layer. The MXY monolayer is composed of three atomic layers stacked in a sequence of X-M-Y as shown in Figure 3 similar to MX_2 [17]. Furthermore, the chalcogen atoms are saturated and thus not very reactive [10]. It is well known that structural symmetry is important in defining the electronic properties of 2D TMD materials [8].

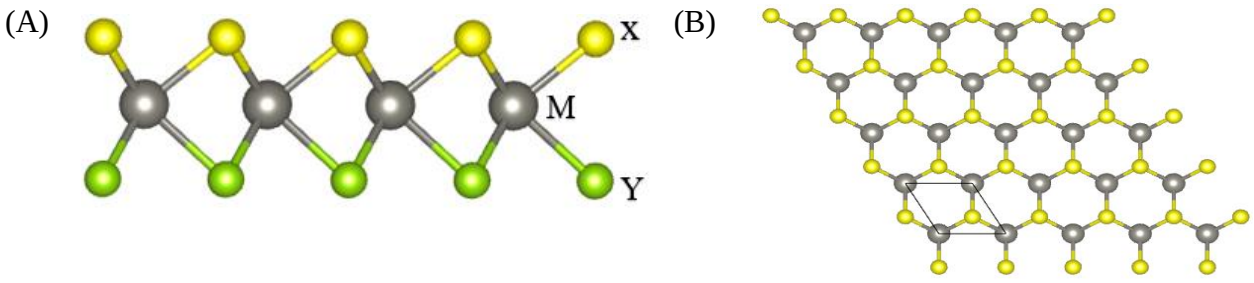

Figure 3. (A) Side and (B) Top Views of JTMD (MXY) Monolayer Atomic Structure (M is Transition metal, X and Y are Dichalcogenides).

The spin-orbit coupling and the band structures of the Janus MXY monolayers, like their parent TMD structure display stable spin splitting at the band margins near the K point [18]. When they come into contact with other materials on different sides, their unique structure allows them to have diverse properties [19]. Potential applications include optoelectronic devices, PV, and solar water splitting [20]. Group-VI Janus chalcogenide MXY includes MoSSe, WSSe, and WSeTe monolayers. Semiconductors of MoSSe and WSSe are direct bandgap monolayers, with the conduction band minimum (CBM) and valence band maximum (VBM) located at the K point in the first Brillouin zone, whereas WSeTe is an indirect bandgap monolayer. The bandgap and electronic properties of TMDs can be tunable through a variety of methods, which include external electric fields, strain engineering, and vertical stacking via van der Waals (vdW) interactions. In this work, first-principles calculations were performed based on DFT to investigate the electronic properties of MoSSe/WSe_2, WSSe/WSe_2, and WSeTe/WSe_2 vdW heterostructures. These results are helpful for potential usage in the application of energy.

1.4 Statement of the Problem

The major sources of electricity production that we utilize are coal and oil, both of which cause large levels of pollution in the atmosphere and environment, are limited in availability, and are dangerous to plant and animal health, among other things. As a result, there is a growing interest and activity in the development and application of alternative/renewable energy sources. In the field of energy technology, for example, the development of more efficient engines, advanced solar photovoltaics, improved batteries, and hydrogen storage all offer opportunities for the potential widespread application of novel materials [21]. Novel materials are developed in response to several different drivers, including the requirement for specific or improved functionality, increased efficiency, and the need to find substitutes for raw materials that are in short supply or have been found to have adverse effects on the environment or human health. The improved efficiency and functionality of novel materials can bring tangible environmental benefits, such as those offered by the development of photovoltaics and fuel cells [21].

This study focuses on novel materials for alternative energy applications, which include PV and water splitting. Atomically thin 2D layered TMDs semiconductor materials have a lot of potential due to their advantageous photon absorption and electrical transport properties. We intended to use MoSSe/WSe_2, WSSe/WSe_2, and WSeTe/WSe_2 vdW heterostructure semiconductors for energy application.

1.5 Objectives

1.5.1 General Objective

To investigate electronic properties of JTMDs/WSe_2 vdW heterostructures using DFT for energy application.

1.5.2 Specific Objectives

- To investigate a stable atomic arrangement of JTMDs and WSe_2 using Geometry optimization.
- To design different stacking of JTMDs/WSe_2 vdW heterostructures.
- To investigate electronic properties of JTMDs monolayers and JTMDs/WSe_2 vdW heterostructures.
- To evaluate the stability, band alignment, and power conversion efficiency (PCE) of different heterostructures for solar cell and water splitting.

1.6 Scope

The scope of this study is to compute the first principle JTMDs/WSe_2 vdW heterostructures using Quantum ESPRESSO and VASP within DFT.

Chapter 2 Literature Review

2.1 Photovoltaic Cell

Currently, fossil fuels such as coal, oil, and natural gas provide the world energy demand [22]. Environmental challenges such as pollution and global warming, as well as energy-related difficulties, are sounding the alarm bell for humanity. The enormous rise in the global population over the previous decade has resulted in a considerable increase in greenhouse gas emissions from fossil fuels [23]. These conventional nonrenewable energy sources are harmful to human health and the environment. This perilous situation, along with the depletion of traditional energy sources, necessitates the development of renewable energy technology. PV, which converts sunlight into electricity, appears to be the most attractive of today's renewable energy technologies. PV cells have an architecture that is based on the union of two semiconductor regions with different electron concentrations (Figure 4) these materials can be type n (semiconductors with an excess of electrons) or type p (semiconductors with an excess of positive charges, known as holes), though the material is electronically neutral in both cases [24].

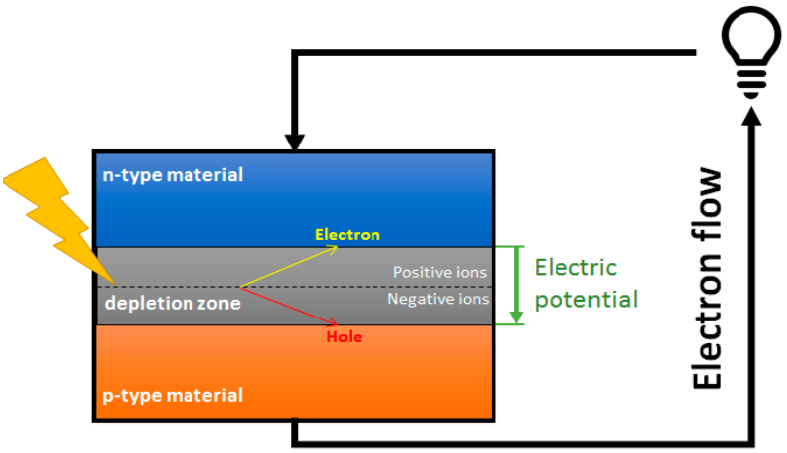

Figure 4. Schematic Representation of a PV Cell with n-type and p-type Layers [24].

When both p and n regions are in contact, holes flow from the p region and electrons from the n region through the p-n junction (diffusion current). When light strikes the cell, the energy contribution of the photons can be absorbed by the electrons, which can break their bonds, producing hole-electron pairs. The electric field pushes these charge carriers, which are then

carried through the p-n junction. An electric current and a potential difference between the cell terminals will be established if an external load is connected [24].

Solar energy has piqued the interest of many people in recent years because of its enormous quantity, low cost, and environmental friendliness [22]. SCs, the device that transforms sunlight into energy, is divided into four generations according to the basic categorization used in PV technology.

2.1.1 First Generation (Wafer Based) Solar Cell

SC of the first generation is manufactured on silicon wafers. Because of its excellent power efficiency, it is the oldest and most common technology. In terms of single-cell PV systems, silicon SCs are the most efficient, and silicon is the most plentiful element on the planet, second only to oxygen. With an energy band gap of 1.1eV, it is a semiconductor material suited for PV applications. Based on how the Si wafers are manufactured crystalline silicon cells are divided into three kinds [24], [25]. The type of silicon determines the kinds utilized, more particularly.

- Monocrystalline (Mono c-Si) [25], [26]
- Polycrystalline (Poly c-Si) [25], [26] and
- Gallium arsenide (GaAs) [24]

Monocrystalline SCs made from thin silicon wafers, which are the oldest, most common, and most efficient SC technology. They have a greater efficiency (up to 25%) than other varieties of solar PV, which means we can get more power from a given area of the panel [24]–[26]. The Czochralski method, which is used in silicon electronics, is used to make single crystal wafers. Because of the bulk purification procedure, the cost of manufacturing single crystalline silicon SCs is high [25]. Polycrystalline silicon is significantly less pure than single crystalline silicon, yet they are the most prevalent due to their low cost. Because of the way silicon is produced, polycrystalline solar panels are cheap than monocrystalline solar panels. Instead of being formed into a single crystal, molten silicon is poured into a mold [25]. The greatest efficiency for a polycrystalline silicon cell has been measured at 20% [24], [25] smaller than (Mono c-Si) based cells. GaAs are obtained by combining Ga and As directly in a vapor-phase reaction at low pressure and high temperature. GaAs-based cells can have several layers with a slightly different composition that allow more accurate control of the generation and collection of electrons and holes than silicon cells, which are limited to

changes in the level of doping to achieve the same results. GaAs production can be divided into four stages: ingot growth, wafer processing, epitaxy, and device fabrication [24]. GaAs cell's efficiencies are in the range of 18.4-28.8% [24], [27] in the laboratory, depending on whether they have a crystalline structure or they consist in a thin layer.

2.1.2 Second Generation Solar Cell

To address the first generation solar SCs issues, the second generation SCs were created, however, their efficiency was not equal to that of the first generation SCs [25]. Thin-film SCs is another name for second-generation SC. Thin-film SCs are made up of thin layers of SCs that are 1 to 4 μm thick and placed onto a broad, cheap substrate like glass, polymer, or metal. Thin films may be packed into lightweight, flexible structures that can be readily incorporated into construction components (building-integrated PV, BIPV). Thin-film SCs have essentially three major kinds that have been commercially produced [25].

- Amorphous silicon (a-Si and a-Si/μc-Si [24]–[26]
- Cadmium Telluride/ cadmium sulfide (CdTe/CdS) [24]–[26] and
- Copper-Indium-Selenide (CIS) and Copper-Indium-Gallium-Diselenide (CIGS) [24], [25]

Amorphous (a-Si) SCs can be made at low temperatures, allowing them to be used on a variety of low-cost polymers and other flexible substrates. The energy required to process these substrates is lower [26]. As a result, a-Si SCs are less expensive and more readily available. In the context of a SC, the term "amorphous" refers to the cell's silicon material, which lacks a defined arrangement of atoms in the lattice is a non-crystalline structure or is not highly organized. These are made by covering the reverse side of the substrate/glass plate with doped silicon material. The reflecting side of these SCs is usually dark brown, whereas the conducting side is silverfish [26]. a-Si is widely used in thin-film SCs owing to several reasons [24], [28].

- Raw materials are abundant and non-toxic;
- It requires low-temperature processes, allowing the manufacturing of modules with a wider and a cheaper range of substrates;
- It presents a high absorption coefficient, hence cells are thinner (of the order of 1–2 μm thick) and require less amount of material per cell;
- Large area deposition technologies can be applied [28]

Laboratory efficiencies of a-Si are 10.2% for single-junction cells and 12.7% for multi-junction cells [24]–[26], [28].

CdTe is a semiconductor compound with a bandgap of 1.45 eV, which makes it a good candidate for converting sunlight into electricity in single-junction cells. CdTe cells achieve lab efficiencies of around 21% [24], [27], and can be obtained mainly by different three routes.

- Direct reaction of Cd and Te at high temperature in a sealed empty quartz tube;
- Exposure of a Cd solution to gaseous H_2Te under an inert atmosphere; and
- Addition of Cd in an alkaline metal telluride solution.

CdTe cells are manufactured by multiple deposition processes that last less than 2.5 h, as schematized in Figure 5: Firstly, a layer of cadmium sulfide (CdS) is vapor-deposited onto a transparent conductive oxide film, front contact [-], which is supported on a heat-treated glass. Then, a CdTe layer is deposited on the CdS layer [24]. A laser-cut that goes through the three layers is made to introduce the insulator into the module. Afterward, several cuts are made with the laser, crossing only the CdS and CdTe layers, to add the rear contact [+] by sputter deposition and later crossing only the back contact layer. Finally, the cell is encapsulated, the wires are connected and the tempered rear glass is placed [24].

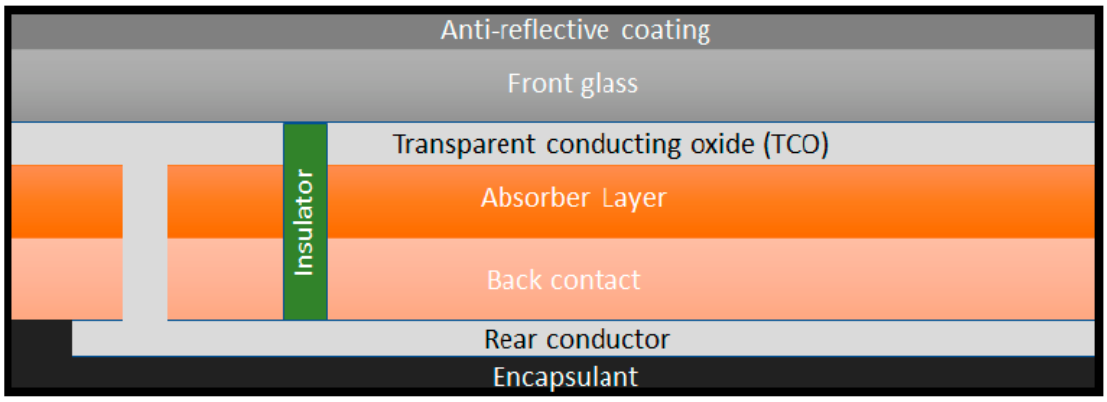

Figure 5. Cross Section of a CdTe Based SC [24].

CdTe PV cells can withstand high temperatures better than c-Si cells and capture radiation better in humid environments. However, the elements that make up the CdTe are scarcer than Si, and CdTe is a potentially toxic material.

Copper, Indium, Gallium, and Selenium are four elements that make up a quaternary compound semiconductor (CIGS) [26], with general formula of Cu $(In_xGa_{1-x})Se_2$ that varies its bandgap value between 1.0–1.7 eV depending on the proportion of the elements in the compound [24]. CIGS-

based SC technology is one of the most likely thin-film technologies due to its considerably high efficiency and economics [26]. CIGS has a better efficiency of 22.3% [24], [29] when compared to CdTe thin-film SCs. CIGS cells are typically manufactured in five steps [24], [29]: (1) A substrate such as Na_2CO_2-CaO, a metal, a ceramic, or a polymer sheet is placed to support the rest of the cell. (2) The substrate is covered with the back contact, which is usually pulverized molybdenum in the form of $MoSe_2$. (3) The CIGS layer (p-type) is grown by a co-evaporation process. (4) A buffer layer (n-type), currently formed by a TCO such as zinc oxide (ZnO) with or without doping is deposited [24], [30]. (5) Finally, an anti-reflective coating is applied to improve cell efficiency. Figure 6 depicts the cross-section structure of a CIGS cell.

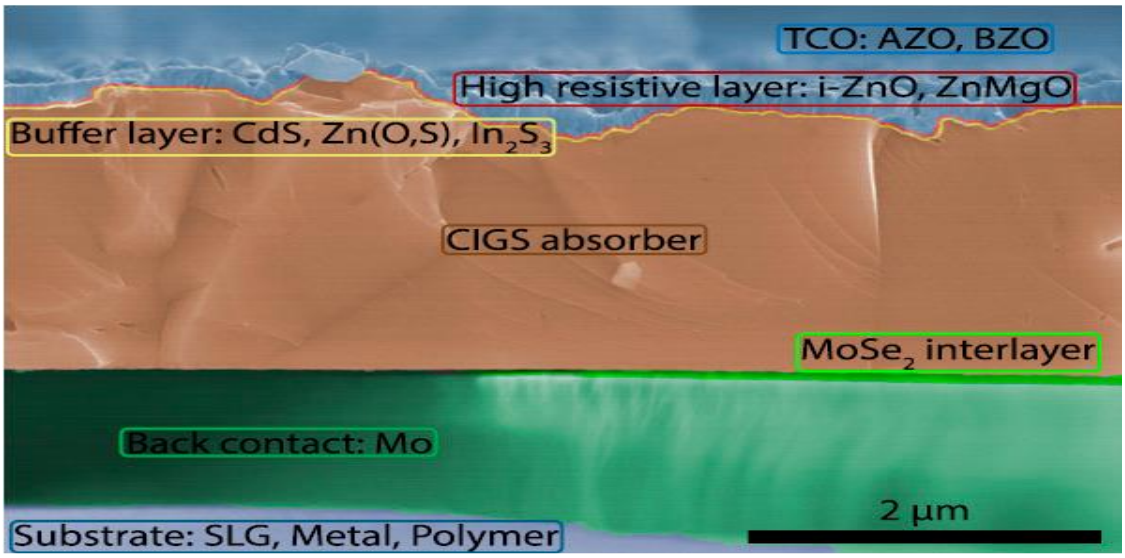

Figure 6. Cross-Section of a CIGS Cell [24].

Although co-evaporation is the most widespread production technique, other techniques such as a one-stage hot wall deposition process are currently being investigated as an alternative to reduce production costs [31]. For instance, the third step can be replaced by the spraying of the CIGS precursor elements followed by selenization and sulphuration, which results in a laboratory efficiency of 22.3% [29]. This would aid to reduce the production cost since the co-evaporation processes require a great deal of energy.

2.1.3 Third Generation Solar Cell

SCs of the third generation are reported to be less costly than SCs of the second generation [22]. Due to its quick energy payback time, third-generation SC, also known as solution-processable solar cells (SPSCs), use molecules or inorganic clusters as main absorbers [23]. The printing

methods of flexible solar panels, which may be readily integrated on the surfaces of inside or exterior building spaces, are used to manufacture SPSCs at a cheap cost. The following are the most important technologies included in third-generation PVs that are dye-sensitized solar cells (DSSCs), organic and polymeric solar cells, perovskite cells, quantum dot cells, and multi-junction cells [24]–[26].

DSSCs are low-cost SCs in the form of thin films based on a semiconductor formed between a photo-sensitized anode and an electrolyte [24]. Since the first DSSC was introduced, many artificial dye molecules have been synthesized, and some of them have been successfully launched into the market such as the so-called N3, N719, and Z907 [24], [32]. The dye molecules must fulfill some requirements, such as matching the solar spectrum, long-term operational stability, and strong attachment to the semiconductor surface. Furthermore, the redox potential must be high enough to facilitate the regeneration reaction with the redox mediator [24], [33]. This type of cell is ideal for low-density applications such as rooftop solar collectors, where the mechanical robustness and light weight of the glass-free collector are a significant benefit. In contrast, they are ineffective for large-scale deployments, where higher-cost, higher-efficiency cells are preferable. DSSCs have several advantages, including the ability to operate in low-light conditions, allowing them to operate under cloudy skies and indirect sunlight, whereas conventional designs would experience a "cut-out" at some lower limit of illumination. Another advantage is the mechanical robustness of the cell, which results in higher efficiencies at higher temperatures, whereas traditional silicon cells experience significant decreases in efficiency as the cells heat up internally. DSSCs typically have only a thin conductive plastic as the front layer, allowing for simple and fast heat dissipation and thus operating at lower internal temperatures. The use of a liquid electrolyte, which has temperature stability issues, is the primary disadvantage of DSSCs. At low temperatures, the electrolyte can freeze, halting power production and frequently causing physical damage. Higher temperatures, on the other hand, cause the liquid to expand, making panel sealing critical [24].

Quantum dots (QDs) are nanoscale semiconductor materials, belonging to groups II-VI, III–V, or IV-VI of the periodic table, that have a discrete spectrum of quantized energy since the movement of the electrons and holes is confined in the three directions of the space. Owing to their nanoscale dimensions, typically between 2–10 nm [24], [34], [35], they exhibit properties that are intermediate between those of bulk semiconductors and those of discrete atoms or molecules. QDs have a structure consisting of a core on which layers of different compounds are deposited to

improve efficiency by reducing interaction forces between the exciton and the surface of the nanoparticle. It is also possible to embed QDs in a matrix of other materials [34]. The conversion efficiency of this type of cell has increased over recent years, being above 11% [24], [36]. This value is difficult to be increased due to the diffusion of charge carriers, thus new cell structures are required, or the combination of QDs technology with other types of cells [37]–[43]. It is also feasible to increase efficiency through doping with other materials [44]; for instance, Si doping can increase efficiency from 11.3% to 17.0%.

Organic photovoltaic cells (OPVCs) are those that use conductive organic polymers or small organic molecules for light absorption and charge transport to produce electricity from sunlight [24]. According to the chemical structure of the electron donor (p-type) semiconductor, OPVCs are classified into two groups: polymer solar cells (PSCs) and small-molecule solar cells. PSCs are typically made of indium tin oxide (ITO) conductive glass that is covered by a polymeric hole transporting layer, an active layer, an electron transport layer, and a metal electrode with a low work function [24]. The highest efficiency reported range between 9.7–11.2% [27], and taking into account the increasing trend found within the last years. P3HT as a donor material yielded the best laboratory performance in OPVCs (22.4%) [45].

Perovskite solar cells (PVSCs) is an ABX_3 crystal structure characterized by a broad optical band gap and high absorption, long carrier diffusion lengths, low recombination losses, cheap material cost, and bandgap tunability [23], [24] e.g. hybrid organic-inorganic lead halide CH_3NH_3Pb (I, Cl, Br)$_3$. Short-term and long-term stability, on the other hand, is one of the main challenges for PVSCs. Their instabilities are primarily caused by environmental moisture and oxygen, thermal influence, heating under and applied voltage, UV and visible lights, and mechanical fragility [46]–[48]. Another significant issue for these cells is that their current-voltage curves exhibit hysteretic behavior depending on the measurement conditions. Several explanations for such behavior have been proposed, including ion movement, polarization, ferroelectric effects, and trap state filling, though the exact cause is unknown [49]. Perovskite cells have improved their efficiency from an initial value of 3.8% in 2009 [50] to 22.13% in 2018 in single-junction architectures [51], [52].

Multi-junction (MJ) SCs are made up of multiple p–n junctions made of various semiconductor materials, each of which produces an electric current in response to different wavelengths of

light, increasing the conversion of incident sunlight into electrical energy and the device efficiency. To take advantage of as many photons as possible, the idea of using different materials with different bandgaps is proposed. The entire cell can be made of the same or different materials, providing a wide range of design options [24]. Overall, despite being highly efficient, MJ solar panels are more expensive than other technologies, implying different applications: In space, MJ solar cells are preferred, whereas c-Si solar cells are better for terrestrial applications. Large-area, cost-effective, and highly reproducible fabrication processes must be developed to expand the use of MJ cells. MJ solar cells, on the other hand, have the potential to have significant penetration in terrestrial applications in concentrator systems.

2.1.4 Fourth Generation Solar Cell

The fourth-generation combines the low cost/flexibility of polymer thin films with the high stability of nanomaterials such as metallic nanoparticles, metal oxides, carbon nanotubes, graphene, and its derivatives [24], [53], [54]. These architectures will retain the benefit of solution-processable devices, resulting in low manufacturing costs, but will also incorporate nanomaterials to improve charge dissociation and charge transport within cells. In particular, special emphasis is placed on graphene, which has emerged as the nanomaterial with the highest scientific and technological expectations. The essence of the nanomaterials in these SCs enables a large volume of surrounding the nanomaterial to be filled using a conductor, such as a polymer [24]. The main advantage of fourth-generation SCs over other technologies is that the combination of organic and inorganic substrates improves solar energy harvesting, resulting in higher efficiency while maintaining significant cost savings [54]. Despite the increasingly obvious improvements in polymer SC performance due to the addition of carbon nanostructures, several issues must be addressed [24].

PV technology is recognized as an essential component of future global energy production and a part of the solution to the growing energy challenge. The preceding description of one to four generations of PV cells, which characteristics, advantages, and limitations of each generation, as well as investigations, have been thoroughly discussed. Table 1 summarizes these technologies, characteristics, and efficiencies achieved.

Table 1. Summary of PV Technologies.

Generations	Technology	Characteristics	Efficiency (%)	References
1st GEN	m-Si	Expensive, stable	24.4	[24], [55], [56]
1st GEN	p-Si	Low cost, high defect content	19.9	[24], [56], [57]
1st GEN	GaAs	Expensive, good design control	18.4-28.8	[24], [56], [58]
2nd GEN	a-Si	Non-toxic, short life cycle	10.2-12.7	[30], [56]
2nd GEN	µc-Si	Low defect content, good degradability	11.9-14.0	[24], [27], [28]
2nd GEN	CIGS	Tunable bandgap	22.3	[24], [27], [29], [31]
2nd GEN	CdTe	High-temperature tolerance	21	[24], [27]
3rd GEN	DSSC	Work in low-light conditions, robustness	5.0-20.0	[24], [32]
3rd GEN	QDs	Efficient conductivity	11.0-17.0	[24], [36]
3rd GEN	OPSCs	The high work function, thermally stable	9.7-11.2	[24], [27], [59]
3rd GEN	PVSC	Cheap, simple	21.1-21.6	[24], [27], [60]
3rd GEN	MJ	Wide range of design, Challenging manufacture	35.8	[24], [27], [61], [62]
4th GEN	PSCs with B-doped CNTs	Improved electron transport	4.1-8.6	[24], [63]

Most first-generation and second-generation technologies are highly standardized and have seen few changes in recent years; they have high efficiencies (20–25%) but are typically expensive [24], though there has been a reduction in the cost of silicon-based cells. On the other hand, the majority of 3rd and 4th generation technologies are in states very close to so-called "basic research"; laboratory prototypes that lead to good results have been developed but have not yet been implemented at an industrial scale [24].

2.2 Van der Waals Heterostructure Based Solar Cell

VdW heterostructures are formed by stacking two or more 2D materials with only vdW interaction in their interlayers but no surface dangling bonds. Because the vdW force in the interlayer is a

long-range weak interaction, and heterostructures can form under large lattice mismatch monolayers [64]. SCs based on heterostructures have high efficiencies and high radiation resistance. The ability of heterostructure photo-converters to efficiently convert highly concentrated sunlight (up to 1000-2000 times [65]) opens up the possibility of a significant (proportional to the degree of concentration) reduction in the area and cost of solar cells and, thus, a reduction in the cost of solar electric power [65]. The vdW heterostructure high-efficiency SC consists of two parts: an absorption layer with a small bandgap and strong light absorption capacity, and a window layer with a large bandgap and high transparency for the incident light. Furthermore, the high carrier mobility and direct bandgap of the absorption layer, which generates photo-generated electrons, are advantageous for increasing the efficiency of SCs. Light-generated carriers can be effectively separated in vdW heterostructures due to their thickness and atomically sharp interfaces. As a result, the probability of electron-hole recombination is extremely low, while the efficiency is high [64]. PCE of some recently reported 2D heterostructure solar cells are listed in Table 2.

Table 2. Calculated Maximum PCE of Some 2D Heterostructures SCs.

System	PCE (%)	References
InSe/Te	13.8	[64]
WSe_2/MoS_2	2.56	[64]
WSe_2/WS_2	2.4	[66]
PN/WSe_2	13.8	[67]
GaTe/InSe	9.1	[67]
MoS_2/p-S	5.23	[67]
GaTe/InS	11.52	[64], [68]
GaTe/GaSe	18.39	[64], [68]

Chemical vapor deposition (CVD) is a promising synthesis approach for vdW heterostructures, where monolayer films are sequentially grown layer-by-layer at high temperatures, with some of the resulting material heterostructures beginning to approach the performance levels of exfoliated crystals. However, the initial investment required and energy cost of CVD growth is high for a given quantity of monolayer material produced [69].

2.2.1 Van der Waals Heterostructure Design

Forming heterostructures of materials is a common strategy to modify the electronic band structures of the materials [70]. As shown in Figure 7, heterostructures made up of different 2D TMDs or JTMDs stacked in an out-of-plane (vertical heterostructure) or in-plane (lateral heterostructure) direction can have significantly different electronic and optical properties than each component material, indicating that they have great potential for different applications.

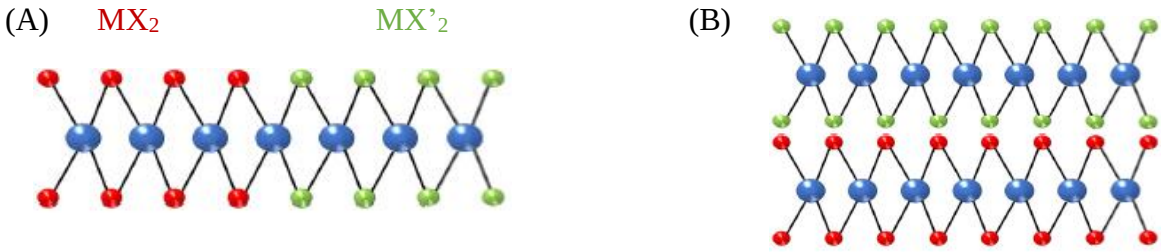

Figure 7. Schematic Illustration of (A) Lateral and, (B) Vertical Heterostructures [71].

Many factors, including stacking order, lattice mismatch, component layers, and so on, can influence the electrical structure of a heterostructure. For example, a direct bandgap is observed in heterobilayers made up of densely stacked distinct monolayer TMDs, where electrons and holes are physically segregated and confined in different layers as shown in Figure 8.

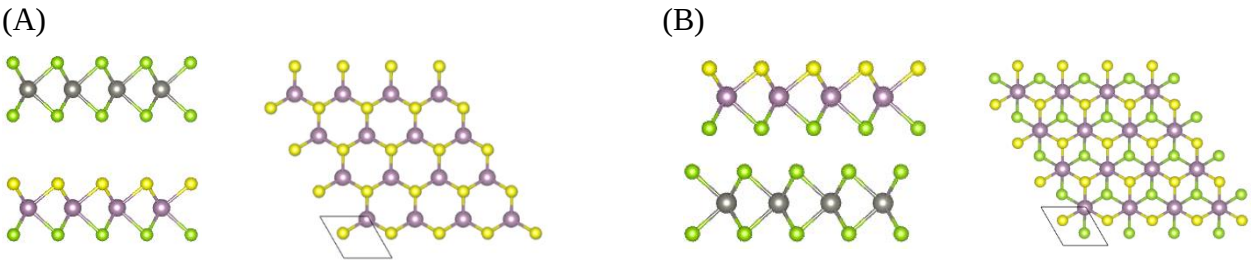

Figure 8. Side and Top Views of Monolayers Stacking Type (A) Stacking AA or Trigonal Prismatic and (B) Stacking AB or Octahedral.

Heterostructures, including TMD bilayers, with well-defined interlayer twist angle, can be achieved by layering one monolayer on top of another. The interlayer twist angle has a considerable influence on the indirect optical transition energy and second-harmonic generation, according to experimental and theoretical studies [70]. Because interlayer twist influences interlayer distance, which governs interlayer interactions and band structures, changing twist angle is available for many applications. A single layer of TMDs or JTMDs can have either trigonal prismatic or octahedral metal coordination (typically distorted and sometimes referred to as

trigonal anti-prismatic) as shown in Figure 8(A) and (B), respectively. One of the two coordination types is thermodynamically favored depending on the metal and chalcogen components combination [9]. The trigonal prismatic phase, also known as the 2H phase (or 1H in the case of a single layer), is defined by a hexagonal symmetry (the D_{3h} group) and corresponds to trigonal prismatic coordination of metal atoms. In addition, the octahedral phase exhibits tetragonal symmetry (D_{3d}) and corresponds to the octahedral coordination of metal atoms. In the design of feasible electronic devices, layer stacking in the form of vdW heterostructures with localization of the valence band maximum (VBM) and conduction band minimum (CBM) to two separate layers (type-II) is widely utilized [72].

2.3 Basic Principles of Photocatalytic Water Splitting

To address global energy and environmental issues, hydrogen production via the water-splitting process is a method of achieving clean and renewable energy. Hydrogen will play an important role in the system because it is the ultimate clean energy and it can be used in fuel cells. Moreover, hydrogen is used in chemical industries. For example, a large amount of hydrogen is consumed in industrial ammonia synthesis. Hydrogen is mainly produced from fossil fuels such as natural gas by steam reforming. Hydrogen has to be produced from water using natural energies such as sunlight. As a result, achieving hydrogen production from water has been encouraged [73].

The water splitting reactions is an uphill reaction with a net Gibbs free energy of 238 kj/mol or 1.23 eV, as shown in Equation (1) [74],

$$O_2 + 4H^+ + 4e^- \rightleftharpoons 2H_2O \text{ Water Oxidation} \quad (2.10)$$

$$4H^+ + 4e^- \rightleftharpoons 2H_2 \text{ Water Reduction} \quad (2.11)$$

$$2H_2O \longrightarrow 2H_2 + O_2 \text{ Water Splitting} \quad (2.13)$$

In general, photocatalytic water splitting on semiconductors entails three major steps: (1) absorption of light irradiation with energies exceeding the semiconductor bandgap, generate electrons (e^-) and holes (h^+) pairs inside the semiconductor particles; (2) the generated electrons and holes are separated followed by migration of these charges to the interface of the semiconductor particles; (3) surface chemical reactions between these carriers with various compounds (e.g. H_2O); electrons and holes to produce H_2 and O_2 respectively as it shown in Figure 9 [74]–[76].

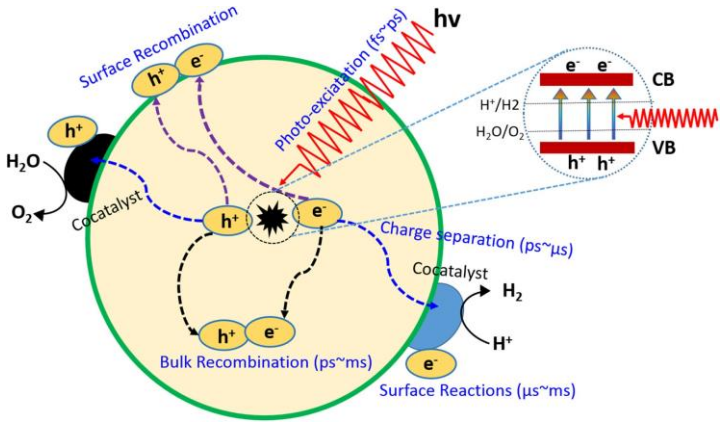

Figure 9. Fundamental Principle of Photocatalytic Water Splitting on Semiconductor [74].

Hydrogen production techniques based on water splitting fall into three categories: photocatalyst systems (PC), photoelectrochemical systems (PEC), and photovoltaic-photoelectrochemical systems (PV-PEC) [77], [78]. In a photocatalytic system (PC), which is thought to be the simplest, cheapest, and potentially scalable method for water splitting. Photocatalyst powders are dispersed in water for water splitting under light irradiation. In the PEC technique, the photocatalysts were initially prepared on conductive substrates as electrodes and an additional small bias was applied for water splitting. To make this cell, one or both electrodes should be a photoactive semiconductor, where the charge separation forms at the semiconductor/liquid interface. Compared to photocatalyst system (PC), PEC has the advantage that there is no need for gas separation in PEC systems because the generation of H_2 and O_2 is spatially separated at different electrode sides [74]. In PV-PEC configuration, the bandgap energy levels in PEC cells have no role with the water redox due to PV cells could play the direct role of potential supply therefore, there are no limitations on selecting the material type [74].

To address PV technology's shortcomings, particularly the high cost of first and second-generation silicon-based SCs, we investigated a new type of SC based on JTMDs and other 2D semiconductors. It is also predicted that the efficiency of vdW heterostructure SCs will increase. In this work, we attempted to use $MoSSe/WSe_2$, $WSSe/WSe_2$, and $WSeTe/WSe_2$ vdW heterostructures, and we studied the electronic properties using first-principle DFT calculation methods for energy applications.

Chapter 3 Methodology

In this study, the electronic properties calculation of Janus MoSSe/ WSe_2, WSSe/ WSe_2, and WSeTe/ WSe_2 vdW heterostructures are performed using plane waves and pseudopotentials based on DFT. DFT is used to study (calculate) the electronic structure of many-body systems in particular atoms, molecules, and condensed phases. The potential for the exchange and correlation is treated by the approximation of generalized gradient (GGA) parameterized by Perdew Berk Ernzed (PBE). PBE employed a combination of exchange and correlation functionals that satisfy many constraints and are very simple to implement.

3.1 Computational Details

All electronic properties of Janus MoSSe/WSe_2, WSSe/WSe_2, and WSeTe/WSe_2 vdW heterostructures first-principle calculations are implemented by quantum ESPRESSO and VASP packages. Quantum ESPRESSO computes the ground state energy and Kohn Sham orbital for various types of structural optimizations. There are three main components of the method, that are PWSCF (plane wave self-consistent field), CP (Car-Parinello), and FPMD (first principle molecular Dynamics). The Kohn-Sham single-particle functions were expanded on a basis of the plane-wave set with a kinetic energy cut-off. Brillouin zone was sampled with 7 × 7 × 1 k-point mesh to get well-converged ground state energy for electronic properties calculations.

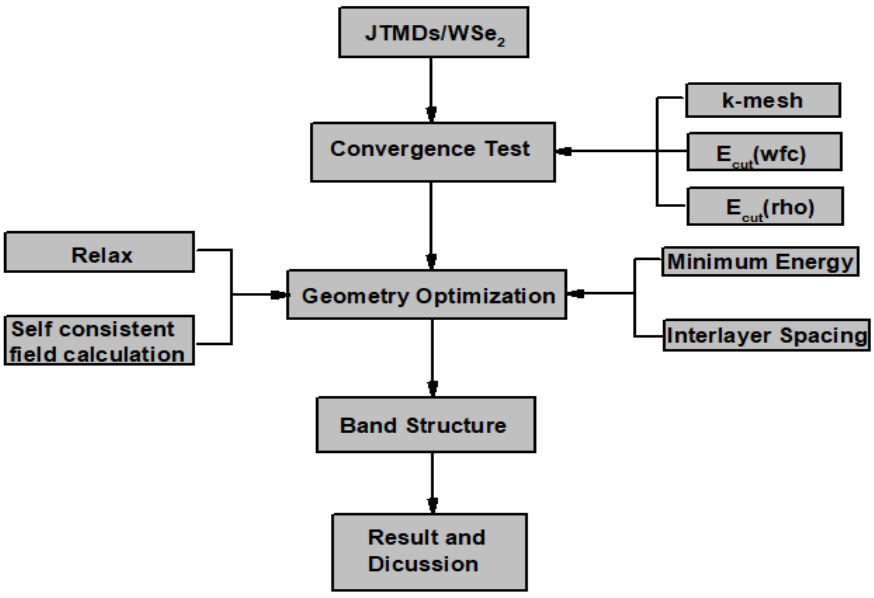

Figure 10. Quantum ESPRESSO and VASP Methods for Calculating Electronic Properties of JTMDs/WSe_2 vdW Heterostructures.

3.2 Density Functional Theory

DFT is one of the most popular and successful quantum mechanical approaches to matter [79]. Which provides an alternative approach to the 'Hartree-Fock plus corrections' paradigm. Unlike Hartree-Fock or extra sophisticated methods (Many-Body Perturbation Theory), based on the wave function, it concentrates on the electron density as the basic quantity.

Hohenberg and Kohn theorem is the heart of DFT [79]. This theorem established total electron density (ρ) completely and exactly which, defines all of the ground-state properties of an N-electron system [80]. The ground-state wave function must not only reproduce the ground-state density but also minimize the energy [79]. The density functional method can be summarized in the following way [80].

$$\rho \Rightarrow V_{ext} \Rightarrow \psi(r_1, r_2, \dots r_N) \tag{3.10}$$

In other words, the electron density (ρ), uniquely defines the external potential, V_{ext}, which has a one-to-one relationship with a unique wave function, ψ, that allows to access all known properties of the system. This, however, is insufficient for the theory to be self-contained; a variational principle is required. Consider multi-electron Schrödinger equation [80]:

$$\left[\sum_{i=1}^{N}\left(-\frac{\hbar^2}{2m_e}\nabla_i^2 + V_{ext}(r_i)\right) + \sum_{i<j}\frac{e^2}{r_i - r_j}\right]\psi(r_1, r_2, \dots r_N) = E\psi(r_1, r_2, \dots r_N) \tag{3.11}$$

Where the first term in the square brackets is the kinetic energy operator and the third term is the inter-electronic repulsion. The first and the last term in the Hamiltonian, which does not involve the external potential, can be cast as a density functional for the total kinetic and columbic interaction energy :

$$F(\rho) = T(\rho) + V_{ee}(\rho) \tag{3.12}$$

A straightforward application of the variational principle gives:

$$F(\rho') + \int V_{ext}\rho' dr \geq F(\rho) + \int V_{ext}\rho dr = E_o \tag{3.13}$$

Where ρ', is not the ρ corresponding to V_{ext}, but some other external potential, and E_o is the exact ground-state energy. Thus, by variationally minimizing the functional $F(\rho)$, the Hohenburg–Kohn variational approach allows a solution of the Schrödinger equation for non-degenerate ground states. Though the functionals $T(\rho)$ and $V_{ee}(\rho)$ formally exist, an exact mathematical form for these density-dependent quantities is not currently known. . Kohn and Sham made important

achievements in this field by mapping the entire interacting system onto a hypothetical non-interacting system in which electrons travel in an effective "Kohn–Sham" single-particle potential. The kinetic energy for the non-interacting system preserves a recognizable form in the Kohn–Sham approach,

$$T_o(\rho) = -\frac{1}{2}\sum_i 2\int \psi_i^*(r_i)\nabla^2\psi_i(r_i)dr \tag{3.14}$$

Where, for simplicity, we assume spin-neutral systems. The non-interacting columbic interaction energy, $J(\rho)$, in the Kohn–Sham approach was also approximated as the classical Coulomb self-energy,

$$J(\rho) = \frac{1}{2}\int\int \frac{\rho(r_1)\rho(r_2)}{r_{12}}\,dr_1 dr_2 \tag{3.15}$$

Kohn and Sham called the error made by these approximations, the exchange-correlation energy E_{XC}.

$$E_{XC}(\rho) = T(\rho) + V_{XC}(\rho) - T_o(\rho) - J(\rho) \tag{3.16}$$

The Kohn–Sham total energy functional hence becomes

$$E(\rho) = T_o(\rho) + \int V_{ext}\rho dr + J(\rho) + E_{XC}(\rho) \tag{3.17}$$

This decomposition is notable since T_o and J for the non-interacting system are provided by known formulas, while the "unknown" functional, E_{XC}, is a relatively small part of the total energy. It is worth noting at this point that because T_o and J are explicitly dependent on ρ, the Kohn–Sham equations must be solved iteratively to self-consistency. There are several computational procedures for producing self-consistent solutions, ranging from simple under-relaxation techniques to complex extrapolation methods [80]. Furthermore, Perdew and colleagues demonstrated that the exchange-correlation energy can be further decomposed as $E_{XC} = E_X + E_C$, where E_X is due to the Pauli principle (exchange energy) and E_C is due to electron correlations. Given the correct exchange-correlation functional, the exact density and total energy of any interacting electronic system can be computed. The correctness and efficiency of such solutions, however, are dependent on approximations to the exchange-correlation functional, $E_{XC}(\rho)$, which we examine in the next section.

3.2.1 Exchange Correlation Functional

The kinetic energy ($T_{non-int}$) of a hypothetical non-interacting system, electrostatic interactions (E_{estat}) of electrons with their charge density, and with nuclear cores account for the (usually) most substantial energetic contributions in density functional theory (DFT) [81].

$$E_{electronic} = T_{non-int} + E_{estat} + E_{XC} \tag{3.18}$$

The system's total energy also includes furthermore the electrostatic repulsion between the nuclear cores. The positions of the nuclear cores are parameters of the electronic Hamiltonian using the Born-Oppenheimer approximation, defining a potential energy surface. The electronic system is assumed to adiabatically follow changes in nuclear coordinates relaxing to its ground state on considerably faster timescales than nuclear motion timescales (electron-phonon coupling, for example, is a correction to this adiabatic approximation). The exchange-correlation energy E_{XC} accounts for the remaining electronic energy not included in the non-interacting kinetic and electrostatic terms. To compute the non-interacting kinetic energy ($T_{non-int}$), an effective potential must be applied to the fictitious particles. The corresponding electrostatic potentials account for the electrostatic interaction terms, and the exchange-correlation potential accounts for E_{XC}.

$$V_{XC}(r) = \frac{\delta E_{XC}(r)}{\delta \rho(r)} \tag{3.19}$$

The exact form of E_{XC} is not known, approximations have to be made [81].

3.2.2 Local Density Approximation

The LDA was one of the earliest techniques for estimating the exchange-correlation energy in bulk solids during the early phases of DFT [80]. In the local density approximation (LDA), the value of E_{XC} $[n(r)]$ is approximated by the exchange-correlation energy of an electron in a homogeneous electron gas of the same density $n(r)$,

$$E_{XC}^{LDA}[n(r)] = \int E_{XC}\big(n(r)\big)n(r)dr. \tag{3.20}$$

Particularly, density $n(r)$, is considered at each point in space and the homogeneous electron gas model is applied locally using the density only. The most accurate data for $E_{XC}\big(n(r)\big)$ is from Quantum Monte Carlo calculations [82]. Despite their simplicity, LDA methods are remarkably precise, especially in systems with slow variations in electron density, such as homogeneous solid metals. The predicted bond lengths, bond angles, and vibrational frequencies in systems where the LDA approach is applicable are comparable to within a few percent of the experimental values. However, many genuine materials are highly inhomogeneous, and the ensuing parameterization in

the LDA technique can lead to serious inaccuracies in predicted properties. Over the years, subsequent improvements have been made to LDA methods in an attempt to correct some of these problems; however, substantial improvements require the implementation of additional variables (and constraints) to address the issues of inhomogeneous electron densities [80].

3.2.3 Generalized Gradient Approximation

The GGA addresses several of the shortcomings of LDA by including extra constraints and terms that account for electron density inhomogeneity [80]. In contrast to the LDA methodology, GGA approaches use both the electron density and density gradients to estimate the real exchange-correlation potential. It is convenient to express the GGA exchange energy as [82]:

$$E_X^{GGA} = E_X^{LDA} - \sum_{\sigma=\alpha,\beta} \int F(s_\sigma)\rho_{\sigma'}^{4/3}(\vec{r})\, d\vec{r}. \tag{3.21}$$

The argument of the function F, s_σ, is the reduced density gradient for spin σ,

$$s_\sigma(\vec{r}) = \frac{|\nabla\rho_\sigma|}{\rho_\sigma^{4/3}(\vec{r})} \tag{3.22}$$

and corresponds to a local inhomogeneity parameter. The GGA functionals have the following general form,

$$E_X^{GGA}[\rho] = \int f((\vec{r}), \nabla\rho(\vec{r}))d\vec{r}. \tag{3.23}$$

There are numerous techniques for incorporating gradients of electron density to develop new GGA functionalities. Perdew and colleagues strongly recommend constructing GGA terms by only adding parameters that satisfy the exact requirements of the exchange-correlation potential [80].

3.3 Quantum-ESPRESSO

Quantum-ESPRESSO is a computer code suite for calculating electronic-structure properties within DFT using a Plane-Wave basis set and pseudopotentials that includes the following core packages [83]:

- PWscf (PW): Plane-Wave Self-Consistent Field,
- CP (CPV): Car-Parrinello Molecular Dynamics

PWscf performs many different kinds of self-consistent calculations of electronic-structure properties within DFT, using a Plane-Wave (PW) basis set and pseudopotentials. In particular:

- Ground-state energy and one-electron (Kohn-Sham) orbitals, atomic forces, stresses;
- Structural optimization, also with variable cell;
- Molecular dynamics on the Born-Oppenheimer surface, also with variable cell;
- Macroscopic polarization and finite electric fields via the modern theory of polarization(Berry Phases);
- The modern theory of orbital magnetization;
- Free-energy surface calculation at a fixed cell through meta-dynamics, if patched with PLUMED.
- Effective Screening Medium (ESM) method
- Self-consistent continuum solvation (SCCS) model, if patched with ENVIRON

The Car-Parrinello (CP) MD is performed by a different code, cp. x. A CP simulation is often made up of a sequence of runs, each one reading data from the one before it. The simulation flow is determined by specifying in the name list & controlling the variables ndr (unit from which data is read), ndw (unit to which data is written), and self-explanatory option restart mode, with possible values: 'from scratch' and 'restart' (and a variant of the latter: 'reset counters', to start or stop accumulating the statistics) [84].

3.4 VASP

VASP (Vienna Ab-initio Simulation Package) is a software program that allows doing ab initio quantum mechanical MD utilizing pseudopotentials and a plane wave basis set [85]. The VASP approach is based on a finite-temperature LDA (with free energy as a variational quantity) and a precise evaluation of the instantaneous electronic ground state at each MD-step using efficient matrix diagonalization schemes and efficient Pulay mixing. These methods avoid all of the issues that arise in the original Car-Parrinello method, which is based on the simultaneous integration of electronic and ionic equations of motion. The interaction of ions and electrons is described using either ultra soft Vanderbilt pseudopotentials (US-PP) or the projector augmented wave approach (PAW). Both strategies allow a considerable reduction of the necessary number of plane waves per atom for transition metals and first row elements. Forces and stress can be easily calculated with VASP and used to relax atoms into their instantaneous ground state.

3.5 Materials Studio and VESTA

Materials Studio and VESTA were used to create bilayer heterostructure of JTMDs and WSe_2. Materials Studio is a modeling and simulation environment designed to allow predicting and understanding the relationships of a material's atomic and molecular structure with its properties and behavior. Materials Studio includes quantum, atomistic (or "classical"), mesoscale, and statistical methods that enable one to evaluate materials at various particle sizes and time scales [86]. In addition, VESTA is a 3D visualization program for structural models, volumetric data such as electron/nuclear densities, and crystal morphologies [87].

3.6 Plane-Wave

To solve the appropriate eigenvalue equation for a periodic system, in the case of Kohn-Sham equations, it requires the use of a basis set to represent the wave function. One of the most commonly used basis sets for calculations on extended systems is the plane-wave basis set, which is a natural choice following the second version of Bloch's theorem. The periodic functions $u_{nk}(r)$ Fourier expanded so that the wave function becomes a sum over plane-waves [88]:

$$\psi_{nk}(r) = e^{ik.r} \sum_{G} C_{n,k} + G e^{iG.r} \tag{3.24}$$

Where the $C_{n,k} + G$ are the expansion coefficients. In principle, this is an infinite sum over the reciprocal lattice vectors, however, in practice, it is possible to truncate the sum so that only those components up to some kinetic energy cut-off, E_{cut}, are included. This truncation is defined by:

$$E_{cut} \leq \frac{|k + G|^2}{2} \tag{3.25}$$

To use such a truncation successfully, the results must be systematically converged concerning the cut-off energy; this convergence of total energy is variational with increasing cut-off energy, which is a special advantage of the plane-wave basis set. Other advantages of plane-waves include their orthogonality and the availability of highly efficient algorithms for their processing, particularly fast Fourier transforms (FFTs), which are used to convert between real and reciprocal space. Furthermore, they are unbiased and cover all spaced evenly, which is useful for calculating forces. However, this is also a disadvantage in that space has a high cost associated with it. Furthermore, when compared to other basis sets, a very large number of basis functions are necessary for correct findings. Finally, plane waves are not a natural choice for the representation of quickly varying functions, which means that the cost of representing the wave function near the ionic cores is

prohibitively high. To overcome this barrier, the pseudopotential approximation is commonly used [88].

3.7 Pseudopotential

A fact of nature is that most physical properties of solids, bonding, for example, depend on the valence electrons to a much greater extent than on the electrons in the core [89]. The pseudopotential approximation makes use of this fact by replacing the strong ionic potential with a weaker pseudopotential that acts on pseudo wave functions instead of on the true wave functions. The concept behind the pseudopotential is illustrated in Figure 11. The valence wave functions oscillate rapidly in the region close to the core. These oscillations occur since the valence wave functions must be orthogonal to the core wave functions, because of the exclusion principle. The pseudo wave functions are then constructed in such a way that they have identical scattering properties of the ions and core electrons as the valence wave functions, but also so that they have no radial nodes in the core region, see Figure 11.

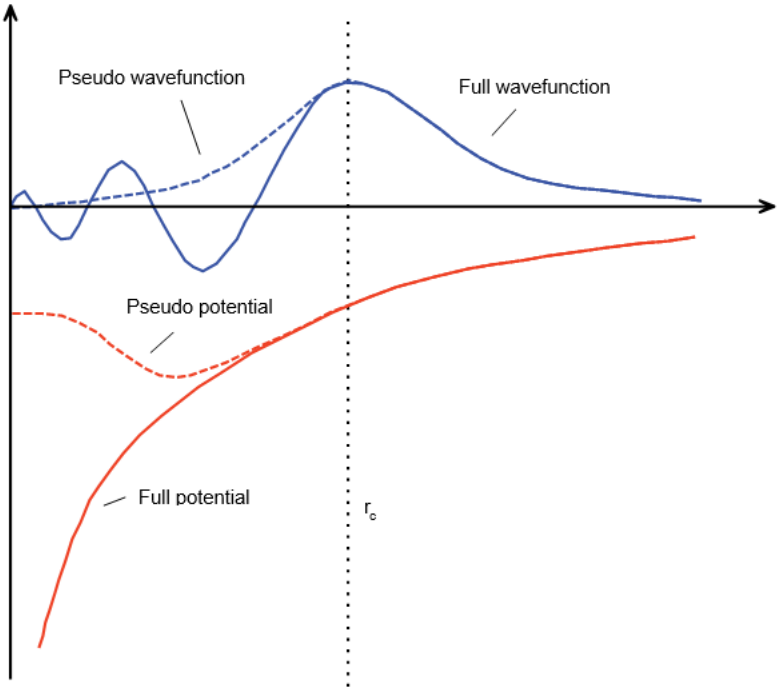

Figure 11. Illustration of the Concept Behind Pseudopotential [89].

Pseudopotentials have been used for a long time in electronic structure calculations. To have a good pseudopotential it is necessary for the potential to be transferable, so that the same potential may be applied to different problems. Norm-conserving pseudopotentials are examples of

potentials that not only have the property that the all-electron and pseudo wave function coincide beyond the cut-off radius but also that the integrated charge inside r_c is identical. These norm-conserving potentials are both accurate and transferable [89].

Chapter 4 Result and Discussion

4.1 Convergence Test

Convergence test is a method of optimizing a simulation to use limited computational resources efficiently and to get meaningful results. It is essential to find a proper initial input setting simulation research to decide the accuracy and reliability of the simulation. To determine an optimized setting for a model, a convergence test is required. DFT obtains a result by using an iterative method and SCF method [90]. SCF calculates ground-state electron density by calculating the energy difference when the electron density is slightly changed. If the energy reaches the global minimum and convergence, the calculation is complete. There are various convergence test methods, but this study focuses on two: the first is to examine energy convergence by changing the cutoff energy, and the second is to check energy by changing k-points [90].

4.1.1 K-Point

The Bloch theorem can be used to show a wave function in a periodic boundary cell.

$$\psi_k(r) = e^{ik.r}u_k(r) \tag{4.10}$$

The wave function is defined in this theorem as k, a vector in the Brillouin zone that represents the smallest polyhedron and is composed of vertical bisectors in the reciprocal space. It possesses point symmetry, similar to a lattice. As we cannot find solutions for an all wave-vector ($\vec{k}$) that exists in the Brillouin zone, we need to calculate some among them through k-point sampling [90].

As shown in Figure 12, the hydrostatic pressure fluctuates depending on the change of k-points and converges. Considering the computing resources, a good set of values selection for WSe_2, MoSSe, WSSe, and WSeTe monolayers is 7*7*1 k-points with a properly small hydrostatic pressure fluctuation.

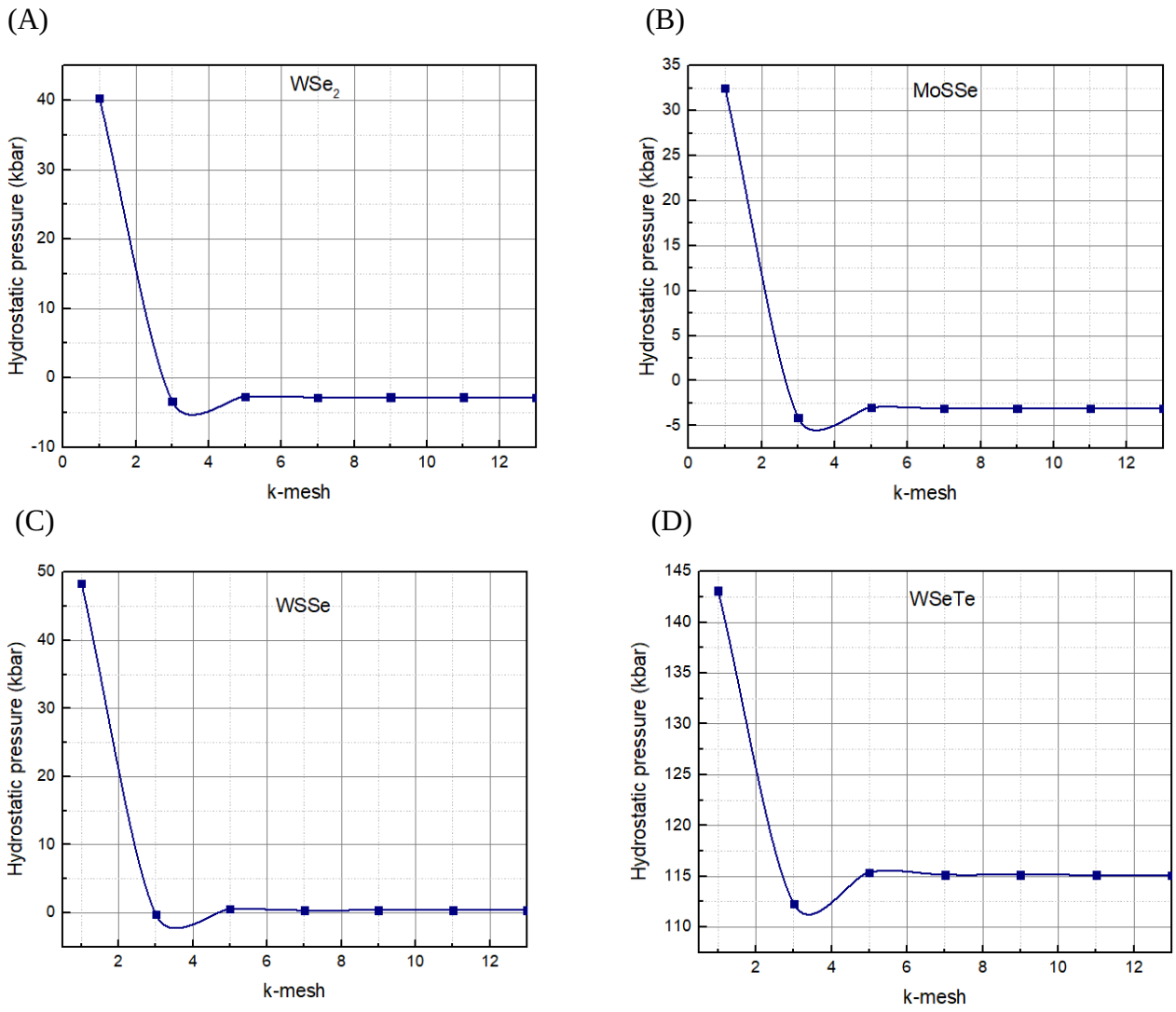

Figure 12. K-mesh vs Hydrostatic Pressure of (A) WSe_2, (B) MoSSe, (C) WSSe, and (D) WSeTe Monolayers Calculated by PBE.

4.1.2 Basis Set Size

In the Quantum ESPRESSO module, if the scripting option is set to General, E_{cut} (wfc), and E_{cut} (rho), which are two keywords concerning cutoff energy, can be found in the & SYSTEM name list. E_{cut} (wfc) indicates the kinetic energy cutoff of wave functions, and E_{cut} (rho) means that of charge density (Unit: Ry). E_{cut} Keyword is to specify the number of plane waves that will be utilized to calculate the DFT. When the value for the calculation of plane waves is set to a high value, the accuracy of the calculation improves, but it takes a longer time to calculate. Thus, adjusting the number of plane waves with the maximum kinetic energy cutoff accurately finds the balance point between the number of plane waves and the calculation time.

It is good to keep E_{cut} (rho) as a multiple of E_{cut} (wfc). We can therefore vary E_{cut} (wfc) first, keeping E_{cut} (rho) at the same factor time's E_{cut} (wfc). Once a good value for E_{cut} (wfc) has been found, the story can be repeated for that multiplication factor.

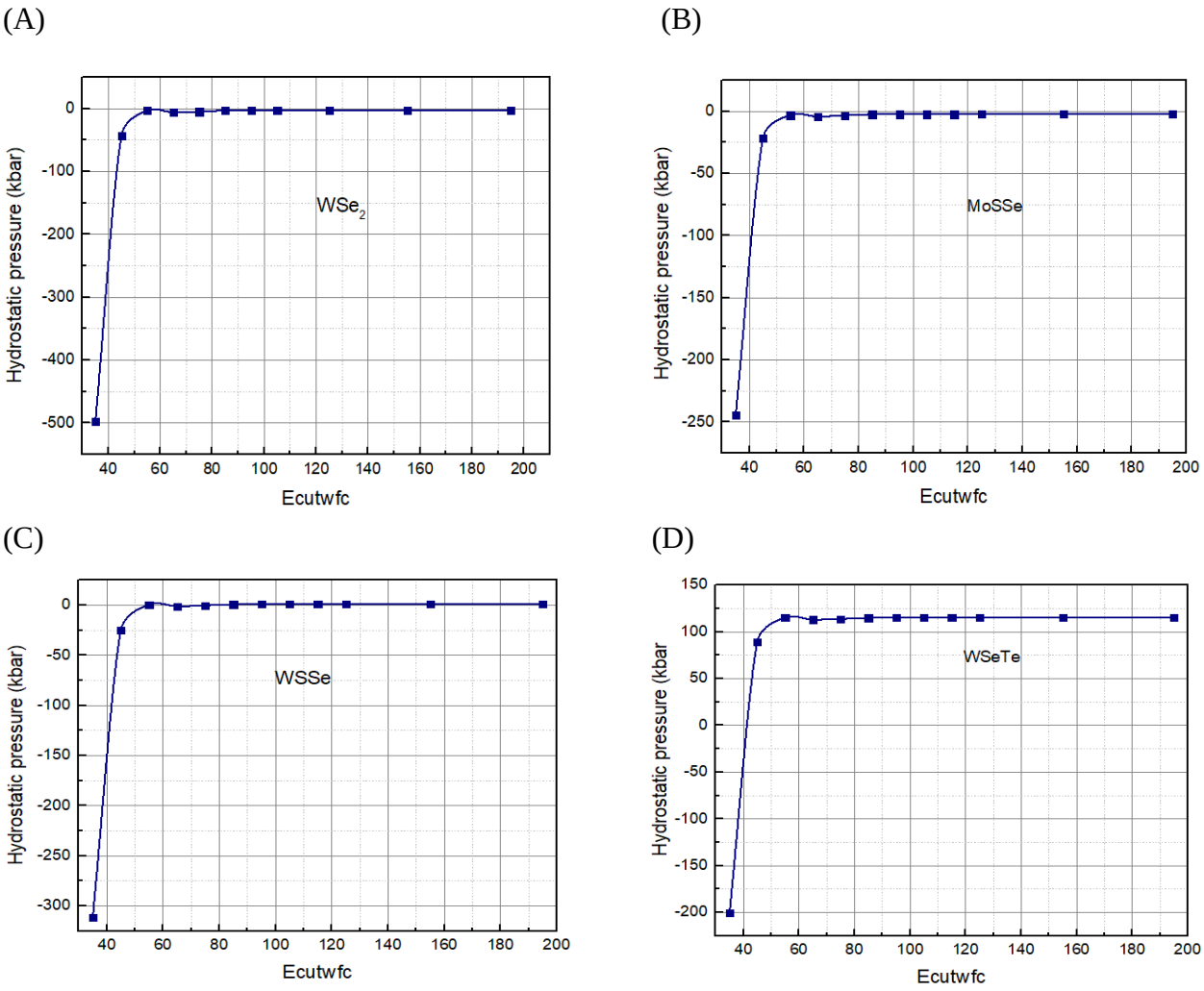

Figure 13. Hydrostatic Pressure vs Ecut (wfc) of (A) WSe_2, (B) MoSSe, (C) WSSe, and (D) WSeTe Monolayers Calculated by PBE.

As shown in Figure 13, the higher the E_{cut} (wfc) and the higher hydrostatic pressure is resulting in convergence. The good set values of E_{cut} (wfc) for WSe_2, MoSSe, and WSSe and WSeTe are 90 Ry, 90 Ry, 95 Ry, and 100 Ry with an appropriately small hydrostatic pressure fluctuation to economize computational resources.

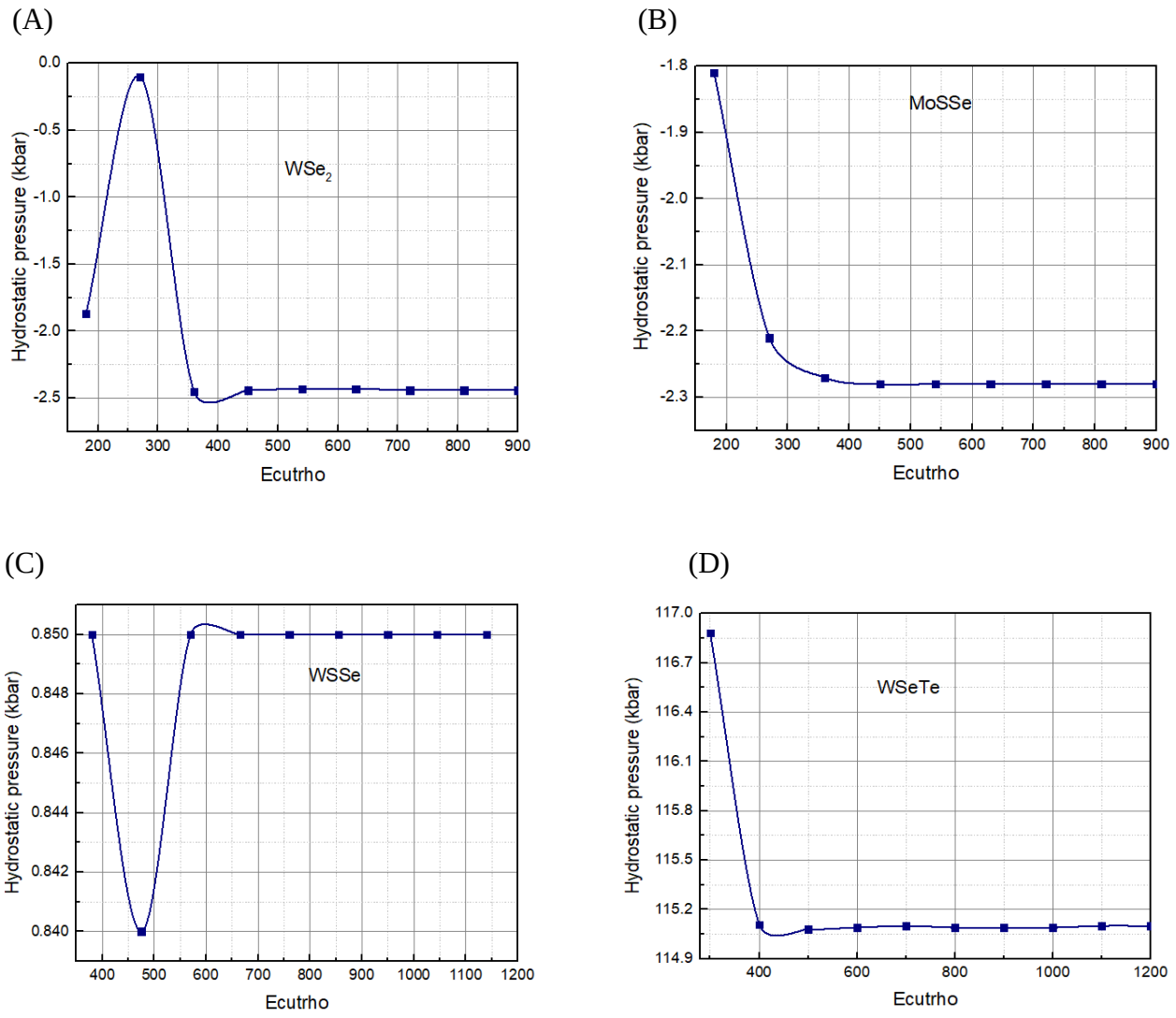

Figure 14. Hydrostatic Pressure vs Ecut (rho) of (A) WSe_2, (B) MoSSe, (C) WSSe, and (D) WSeTe Monolayers Calculated by PBE.

The graphs show in Figure 14, the higher E_{cut} (rho) and the smaller hydrostatic pressure difference between two consecutive measurements show convergence for WSe_2, MoSSe, and WSeTe monolayers but, for WSSe monolayer convergence result is higher E_{cut} (rho) and the higher hydrostatic pressure. The good set values of E_{cut} (rho) for WSe_2, MoSSe, and WSSe and WSeTe monolayers are 600 Ry, 600 Ry, 800 Ry, and 600 Ry.

4.2 Optimized Structure of MXY and WSe_2 Monolayers

Before constructing 2D MXY/WSe_2 heterostructures, geometrical structures of monolayers must be optimized. MoSSe, MoSTe, MoSeTe, WSSe, WSTe, and WSeTe are Janus MXY monolayers used to design vdW heterostructures. Lattice mismatch is required to form the most stable

heterostructures using 2D semiconductors. Well-matched structural nature is beneficial for the assembly of vdW heterostructures. Therefore, we have optimized lattice parameters, minimum energy, and lattice mismatch of WSe_2 and Janus MXY monolayers by using the GGA-PBE method as shown in Table 3. The calculated lattice mismatch ($\Delta a/a_{substrate}$) is expressed by [91]:

$$\frac{\Delta a}{a_{substrate}} = \frac{a - a_{substrate}}{a_{substrate}} \times 100\% \quad (4.11)$$

Where $a_{substrate}$ is the lattice constant of the substrate.

Table 3. Lattice Parameters, Minimum Energies, and Lattice Mismatch of Monolayers Calculated Using PBE.

Monolayers	Lattice Parameter (Å)	Minimum Energy (eV)	Lattice Mismatch (%)
WSe_2	3.34	-21280.469	
MoSSe	3.26	-11323.199	2.39
MoSTe	3.36	-10789.068	0.59
MoSeTe	3.43	-15353.921	2.69
WSSe	3.26	-16715.765	2.39
WSTe	3.27	-34480.374	2.09
WSeTe	3.45	-20746.368	3.19

When the lattice mismatch $|\Delta a/a_{substrate}|$ is less than 5%, the two layers are completely coherent [91]. The lattice mismatch of MoSSe/ WSe_2, WSSe/ WSe_2, and WSeTe/ WSe_2 is 2.39%, 2.39%, and 3.19% respectively, which are quite small, more likely to form heterostructures in terms of the vdW interactions and indicates it is possible to fabricate the structures experimentally. Since no strong interaction exists between MoSSe/ WSe_2, WSSe/ WSe_2, and WSeTe/ WSe_2, the weak vdW interaction will play a major role. Though the other heterostructures have also a small lattice mismatch, it was challenging to form suitable stacking with materials studio. Therefore, we did not study them further. According to the lattice mismatch MoSSe/ WSe_2, WSSe/ WSe_2 and WSeTe/ WSe_2 vdW heterostructures were studied through first-principle calculations.

4.3 Geometry Optimization

The objective of geometry optimization is to generate the optimal (lowest energy) molecular structure from any starting state. Geometry optimization explains Quantum ESPRESSO can be used to determine the geometry of the ground state. Using E_{cut} and k-points will provide extra information on top of the ground state geometry. The shape of the unit cell of monolayers and Janus heterostructures can be optimized using lattice parameters. Where the lattice parameter a (= the 'A' value under & SYSTEM) is varied in steps of 0.01 Å above and below the initial value. This means rescaling the unit cell (growing and shrinking), without altering its shape. The coordinates of all internal positions are also kept constant.

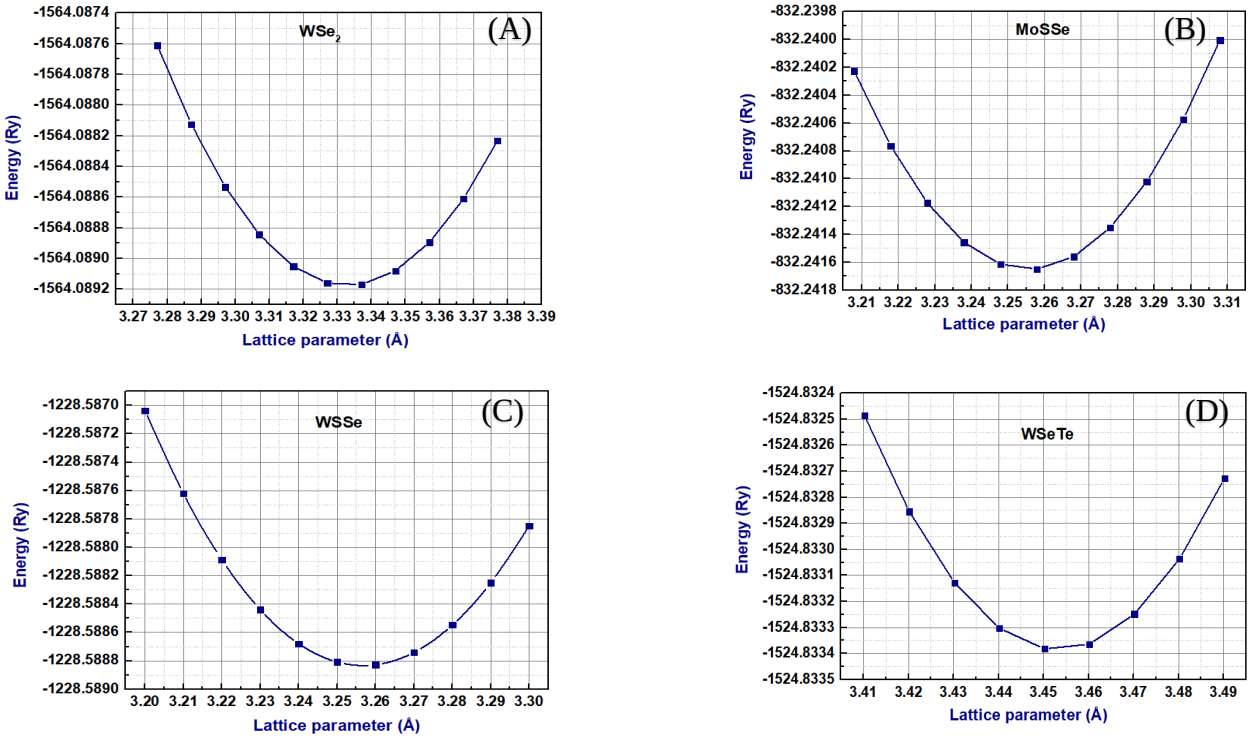

Figure 15. Energy vs Lattice Parameter of (A) WSe_2, (B) MoSSe, (C) WSSe and, (D) WSeTe Monolayers Calculated Using PBE.

Figure 15, shows the energy minimization concerning the lattice parameter of each of the structures under consideration. The vertical axes shifted so that the minimum energy value obtained lies on the horizontal axis. The minimum energy of WSe_2, MoSSe, WSSe, and WSeTe monolayers are -21280.47 eV, -11323.19 eV, -16715.76 eV, and -20746.37 eV with a lattice constant of 3.34 Å,

3.26 Å, 3.26 Å, and 3.4502 Å. For each MXY/WSe_2 heterostructure, eight possible stacking patterns were examined as shown in Figure 16.

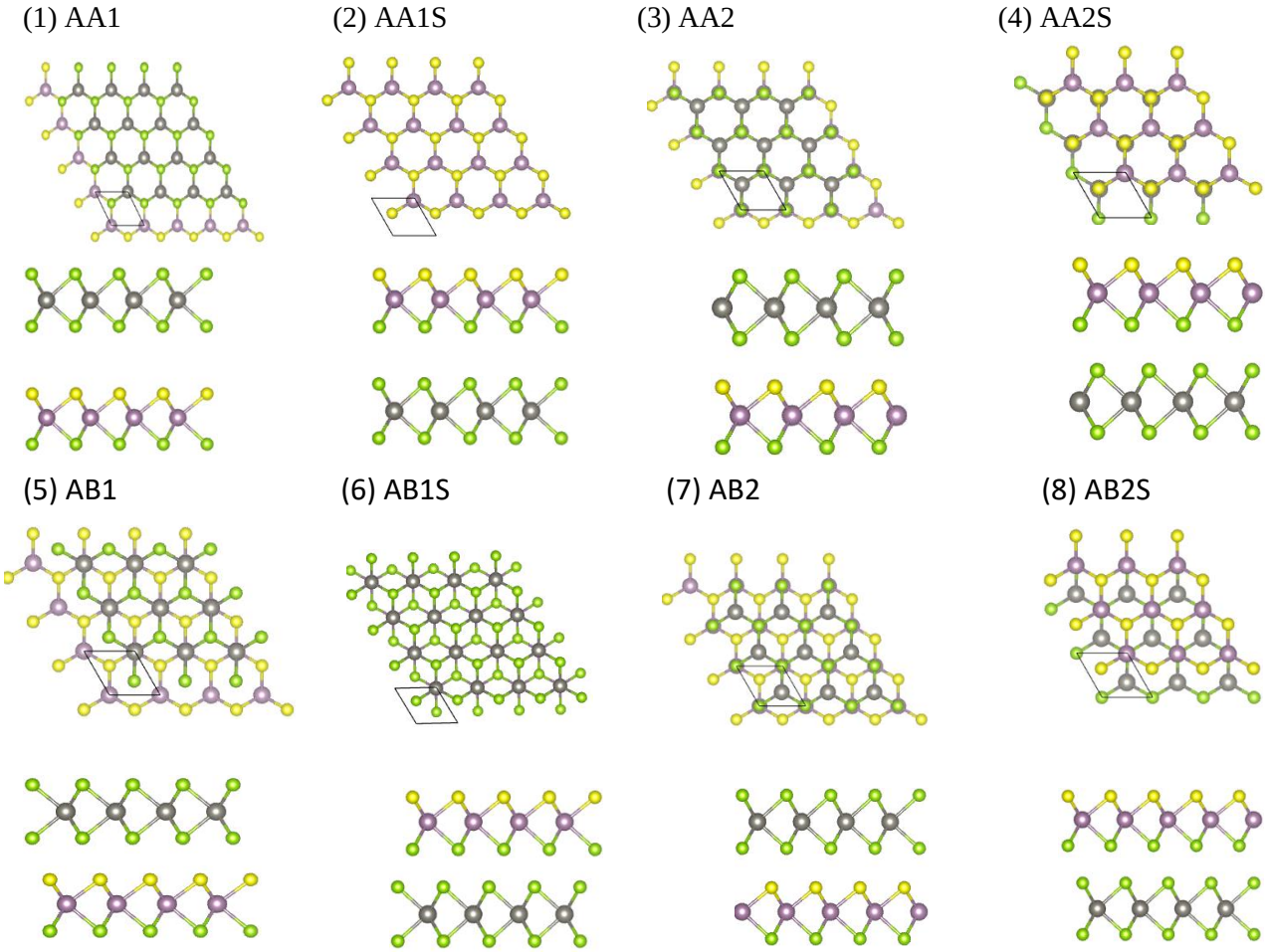

Figure 16. MXY/WSe_2 vdW Heterostructures in Eight Possible Stacking Sequences.

Different stacking modes are obtained by translating, inverting, and rotating one monolayer concerning the other to find the most stable vdW heterostructures. The stability of the heterostructures is determined by the binding energy E_b [92]. The formula of the binding energy is:

$$E_b = E - E_1 - E_2 \tag{4.12}$$

Where E is the total energy of the heterostructure, E_1 is the energy of the isolated MoSSe/ WSeTe / WSSe monolayer E_2, is the isolated WSe_2 monolayer's energy. Table 4 shows heterostructures of MoSSe/WSe_2 with different stacking patterns, as well as lattice parameters, interlayer distance, and binding energies.

Table 4. Lattice Parameters, Interlayer Distances, and Binding Energies of MoSSe/WSe_2 vdW Heterostructures Calculated Using PBE.

Stacking Patterns	Lattice Parameter a = b (Å)	Interlayer Distance (Å)	Binding Energy (eV)
AA1	3.288	4.33690 (Se-S)	-0.1185
AA1S	3.288	3.53396 (Se-Se)	-0.1653
AA2	3.288	4.13729 (Se-Mo)	-0.1102
AA2S	3.288	4.19335 (Se-W)	-0.1667
AB1	3.298	5.82003 (W-Mo)	-0.1751
AB1S	3.308	5.74679 (W-Mo)	-18216.7536
AB2	3.288	4.02844 (Se-Mo)	-0.1502
AB2S	3.298	4.15082 (Se-Mo)	-18192.8921

The binding energies of WSSe/WSe_2 heterostructures eight stacking patterns along with lattice parameter and interlayer distance are illustrated in Table 5.

Table 5. Lattice Parameters, Interlayer Distances, and Binding Energies of WSSe/WSe_2 vdW Heterostructures Calculated Using PBE.

Stacking Patterns	Lattice Parameter a = b (Å)	Interlayer Distance (Å)	Binding Energy (eV)
AA1	3.29	3.50151 (Se-S)	-0.2009
AA1S	3.29	3.51108 (Se-Se)	-0.1884
AA2	3.29	4.00409 (Se-W)	-0.2285
AA2S	3.29	4.05524 (Se-W)	-38995.6907
AB1	3.30	5.61858 (W-W)	-0.2156
AB1S	3.31	5.72509 (W-W)	-0.1172
AB2	3.29	4.00953 (Se-W)	-0.2470
AB2S	3.30	4.08838 (Se-W)	-0.2089

The heterostructures of WSeTe/WSe_2 different stacking patterns are described in Table 6 along with lattice parameters of stacking pattern, interlayer distance, and binding energy.

Table 6. Lattice Parameters, Interlayer Distances, and Binding Energies of $WSeTe/WSe_2$ vdW Heterostructures Calculated Using PBE.

Stacking Patterns	Lattice Parameter a = b (Å)	Interlayer Distance (Å)	Binding Energy (eV)
AA1	3.4302	3.56765 (Se-S)	-0.1774
AA1S	3.4302	3.55108 (Te-Se)	-0.1654
AA2	3.4402	3.93341 (Se-W)	-0.1513
AA2S	3.4402	4.75952 (W-Te)	-0.3296
AB1	3.4502	5.80188 (W-W)	-0.2210
AB1S	3.4902	5.37591 (W-W)	0.3062
AB2	3.4402	3.93356 (Se-W)	-0.1723
AB2S	3.4702	3.83970 (Se-W)	0.3449

The most stable stack modes of $MoSSe/WSe_2$, $WSSe/WSe_2$, and $WSeTe/WSe_2$ heterostructures are presented in Figure 17.

(A) AB1S-$MoSSe/WSe_2$ (B) AA2S-$WSeTe/WSe_2$ (C) AA2S-$WSSe/WSe_2$

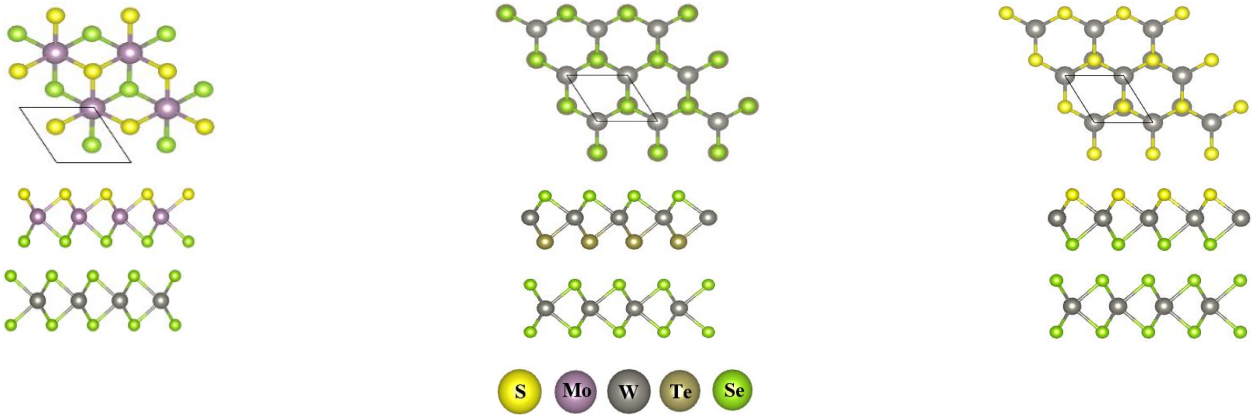

Figure 17. Top and Side Views of the Most Stable Stacks Modes vdW Heterostructures (A) $MoSSe/WSe_2$, (B) $WSeTe/WSe_2$, and (C) $WSSe/WSe_2$.

The binding energy of the $MoSSe/WSe_2$, $WSSe/WSe_2$, and $WSeTe/WSe_2$ heterostructures are -18216.75 eV, -38995.69 eV, and -0.3296 eV respectively, while the bond lengths of W-Se, Mo-S, Mo-Se, W-S, and W-Te are 2.5 Å, 2.4 Å, 2.5 Å, 2.4 Å, and 2.64 Å respectively, indicating the typical vdW nature of the interaction between the two layers. As shown in Figure 18, the interlayer

spacing/distance for $MoSSe/WSe_2$, $WSSe/WSe_2$, and $WSeTe/WSe_2$ are 5.75 Å, 4.05 Å and 4.72 Å respectively.

(A) (B) (C)

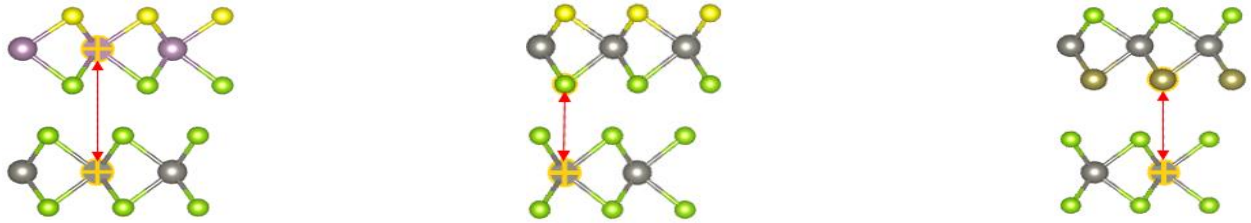

Figure 18. Side View of (A) $MoSSe/WSe_2$, (B) $WSSe/WSe_2$, and (C) $WSeTe/WSe_2$ Heterostructures Interlayer Spacing.

As the lattice parameter was increased from the starting point, the free energy of the unit cell reached a minimum and then increased as the lattice parameter was increased further, as shown in Figures 19 and 20. The most stable stacking vdW heterostructures of $MoSSe/WSe_2$, $WSSe/WSe_2$, and $WSeTe/WSe_2$ minimum energies are -32603.52 eV, -37996.18 eV, and -42026.83 eV at the lattice parameter of 3.308 Å, 3.29 Å, and 3.4402 Å respectively.

(A) (B)

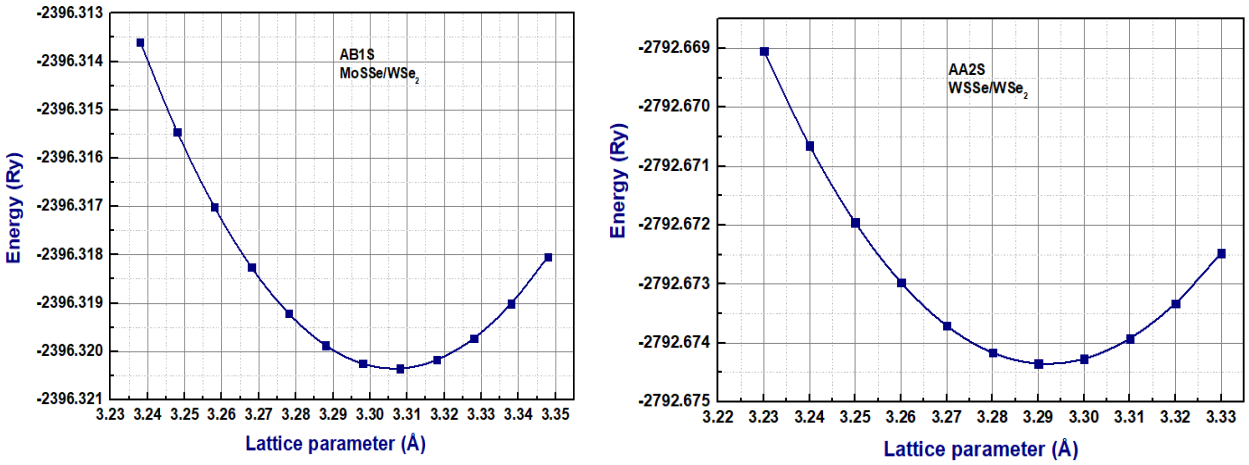

Figure 19. Energy vs Lattice Parameter of (A) $MoSSe/WSe_2$, and (B) $WSSe/WSe_2$ vdW Heterostructures Calculated Using PBE.

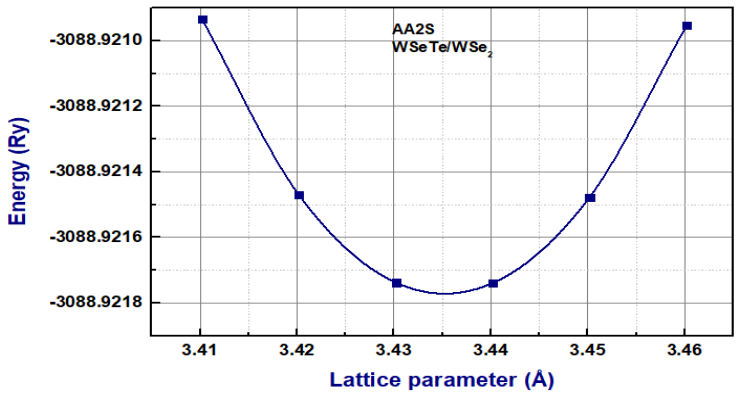

Figure 20. Energy vs Lattice Parameter of $WSeTe/WSe_2$ vdW Heterostructure Calculated Using PBE.

4.4 Electronic Properties of $MoSSe/WSe_2$, $WSSe/WSe_2$, and $WSeTe/WSe_2$ vdW Heterostructures

Electronic band Structure is one of the most fundamental properties of a material and is the foundation for understanding its various properties. The different stacking orders and interlayer interaction are expected to have a significant effect on the electronic properties of $MoSSe/WSe_2$, $WSSe/WSe_2$, and $WSeTe/WSe_2$ heterostructures.

The projected band structures of the $MoSSe/WSe_2$, $WSSe/WSe_2$, and $WSeTe/WSe_2$ vdW heterostructures are shown in Figure 21, 22, and 23. $MoSSe/WSe_2$ and $WSeTe/WSe_2$ are type-II band alignment semiconductors with a direct bandgap of 1.2424 and 0.9527 eV respectively. The CBM and VBM of the $MoSSe/WSe_2$ and $WSeTe/WSe_2$ heterostructures are located at the *K* point in BZ. Moreover, both the CBM and VBM of these two heterostructures originate from the TMD layer. The $WSSe/WSe_2$ heterostructure is also a type-II band alignment semiconductor with an indirect bandgap of 1.3331 eV. The WSSe or WSe_2 layers predominately contribute to the CBM and VBM of the $WSSe/WSe_2$ heterostructure.

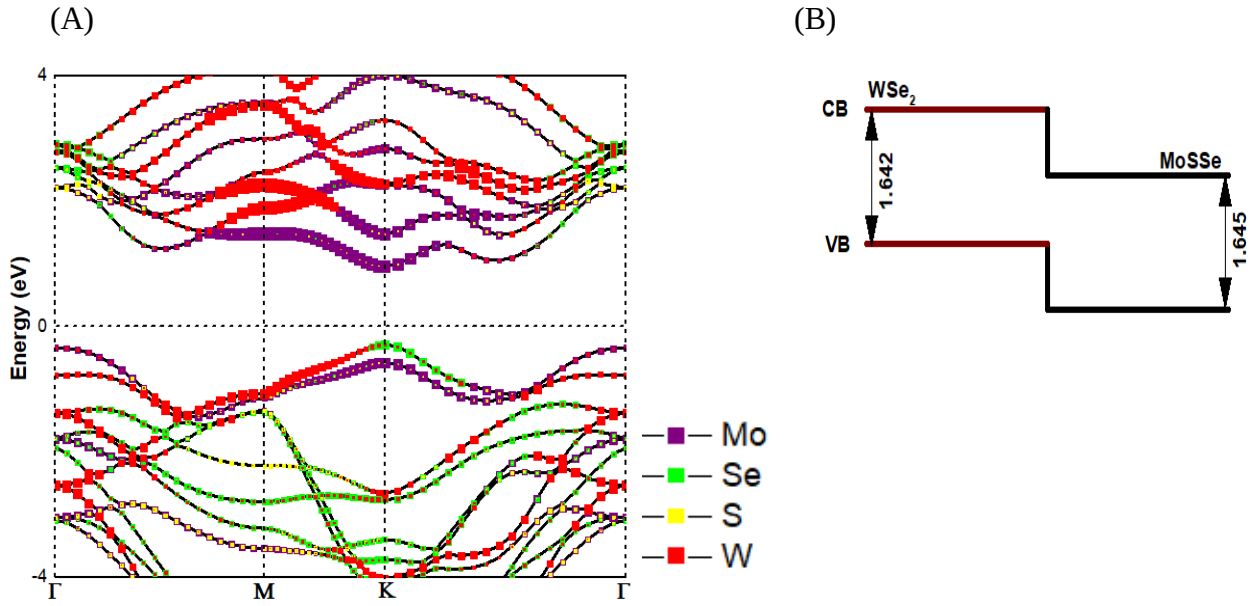

Figure 21. (A) Band Structure and (B) Type-II Band Alignment of MoSSe/WSe_2 vdW Heterostructure Calculated Using PBE.

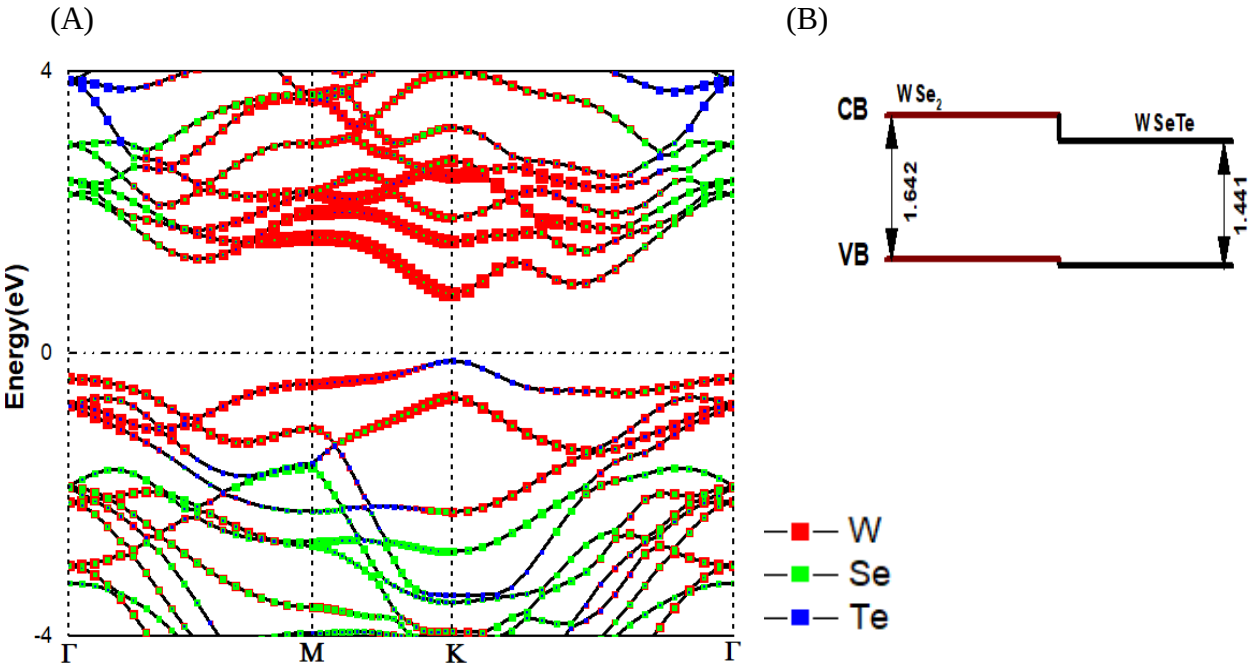

Figure 22. (A) Band Structure and (B) Type-II Band Alignment of WSeTe/WSe_2 vdW Heterostructure Calculated Using PBE.

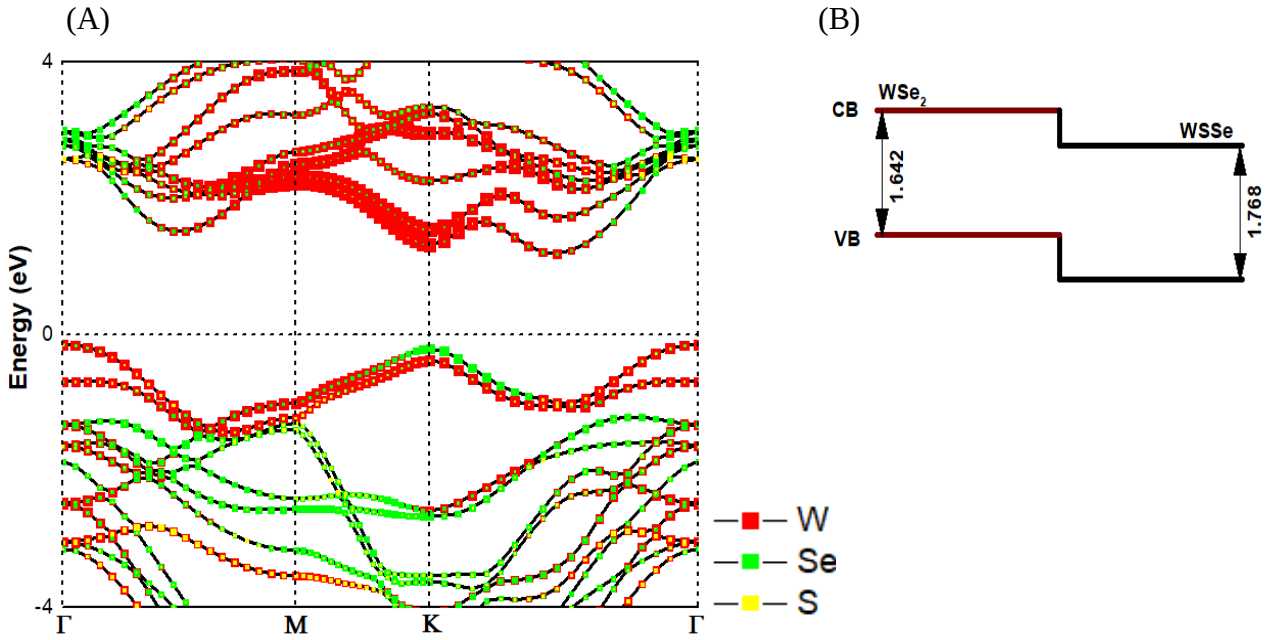

Figure 23. (A) Band Structure and (B) Type-II Band Alignment of WSSe/WSe_2 vdW Heterostructure Calculated Using PBE.

Photo-excited electrons and holes transfer in type-II vdW heterostructures are advantageous for photo energy detection and harvesting. Photon absorptions in a type-II heterostructure generate the excited free carriers. In an ultrafast time scale, free carriers split into electrons and holes at the donor and acceptor. During the free carrier dissociation process, electrodes will generate photocurrent [93].

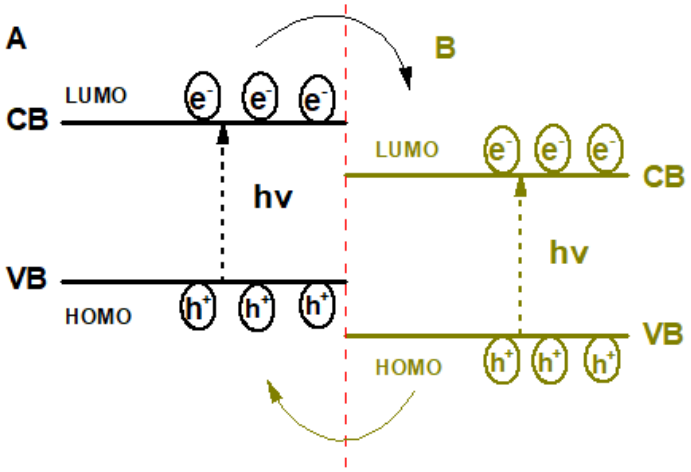

Figure 24. Band Alignment of Heterostructure Semiconductor with Staggered Gaps (Type II) for SCs.

As shown in Figure 24, semiconductor (**A**) CB and VB levels are higher than semiconductor (**B**) comparable levels. Thus, under light irradiation, electrons in the CB of semiconductor **A** can be transferred to that of semiconductor **B**, while holes in the VB of semiconductor **B** can be transferred to that of semiconductor **A**. As a result, the spatial separation of electron-hole pairs is possible [94]. Type-II donor-acceptor interface band heterostructures can easily increase electron and hole carrier transport and separation at the interface, which can greatly improve PV SC efficiency. Electronic band structures of $MoSSe/WSe_2$, $WSSe/WSe_2$, and $WSeTe/WSe_2$ vdW heterostructures as shown in Figures 21, 22, and 23 respectively show that all of them exhibit type II band alignment with the advantages of the separation of electron-hole pairs. Moreover, total DOS of $MoSSe/WSe_2$, $WSeTe/WSe_2$, and $WSSe/WSe_2$ vdW Heterostructures are shown in Figure 25. DOS is essentially the number of different states at a particular energy level that electrons are allowed to occupy, i.e. the number of electron states per unit volume per unit energy [95].

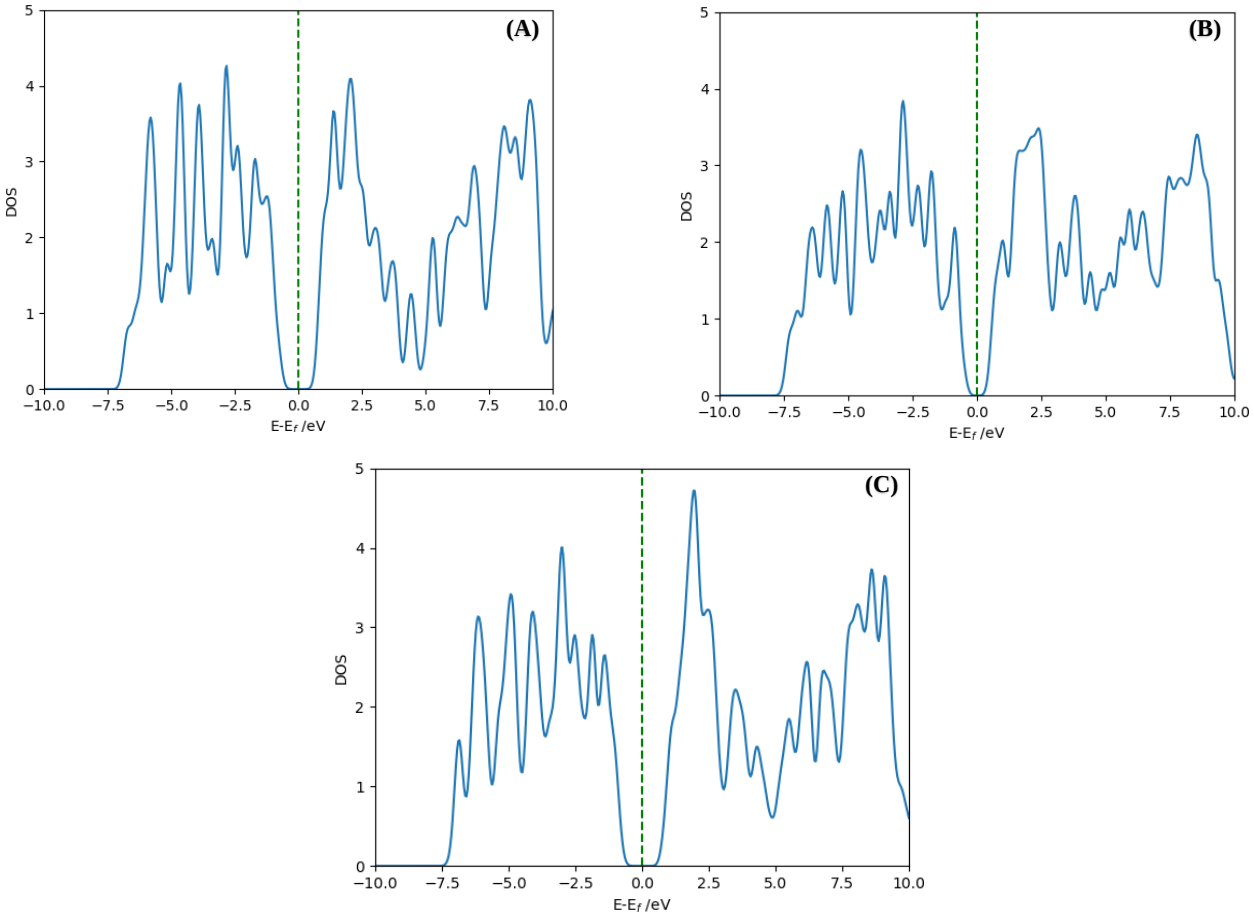

Figure 25. Total DOS of (A) $MoSSe/WSe_2$ (B) $WSeTe/WSe_2$, and (C) $WSSe/WSe_2$ vdW Hetrostructures Calculated Using PBE.

The electronic properties of individual monolayers, as well as $MoSSe/WSe_2$, $WSSe/WSe_2$, and $WSeTe/WSe_2$ vdW heterostructures are summarized in Table 7.

Table 7. Electronic Properties of Individual Monolayers as well as $WSeTe/WSe_2$, $WSSe/WSe_2$, and $MoSSe/WSe_2$ vdW Heterostructures Calculated Using PBE.

Monolayers and heterostructures	Bandgap (eV)	Vacuum-Level (eV)	Electron Affinity (eV)	Ionization Energy (eV)
WSe_2	1.642 (Direct)	3.577	-3.431	-5.073
MoSSe	1.645 (Direct)	4.421	-4.234	-5.880
WSSe	1.768 (Direct)	3.960	-3.885	-5.653
WSeTe	1.441 (Indirect)	4.344	-3.718	-5.158
$MoSSe/WSe_2$	1.242 (Direct)	6.002	-4.400	-5.642
$WSSe/WSe_2$	1.333 (Indirect)	5.661	-4.187	-5.520
$WSeTe/WSe_2$	0.953 (Direct)	5.928	-4.191	-5.144

4.5 Power Conversion Efficiency

To evaluate the quality of $MoSSe/WSe_2$, $WSSe/WSe_2$, and $WSeTe/WSe_2$ vdW heterostructures estimated the power conversion efficiency (PCE) given by Scharber equation [96].

$$\eta(E_g) = \frac{FF \times J_{SC} V_{OC}}{P_{sun}} \tag{4.13}$$

The appropriate value for heterostructure Fill Factor (FF) and potential loss are 0.57 and 0.3. The solar PCE of type-II $MoSSe/WSe_2$, $WSSe/WSe_2$, and $WSeTe/WSe_2$ vdW heterostructures is calculated to be 20.16%, 20.48%, and 19.05%, respectively.

The result illustrates our materials are a promising candidate for solar cell applications.

4.6 Photocatalysis

One of the important prerequisites for water splitting is the straddling of the reduction potential of hydrogen and the oxidation potential of water by the conduction and valence band edges. The width of the bandgap and the levels of the conduction and valence bands are critical parameters in semiconductor photo-catalyst materials [97]. The band edges need to straddle the reduction and oxidation potential of water at a particular pH value for the simultaneous occurrence of hydrogen and oxygen evolution reactions (OERs) via photocatalytic water splitting [97]. A large number of

heterogeneous photocatalysts have semiconductor characteristics. Photocatalytic reaction processes occur on semiconductor materials, as shown schematically in Figure 26. Semiconductors have a band structure with the conduction band separated from the valence band by an appropriate bandgap [73].

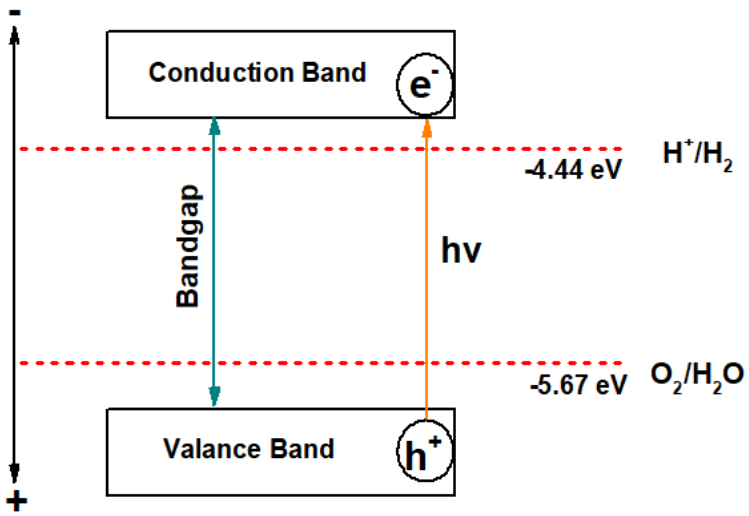

Figure 26. Water Splitting Principle Using Semiconductor Photocatalysts.

When the incident light energy exceeds the bandgap, electrons and holes are generated in the conduction and valence bands, respectively. The photo-generated electrons and holes cause redox reactions similarly to electrolysis. For overall water splitting, electrons reduce water molecules to generate H_2 and holes oxidize water molecules to form O_2. The width of the bandgap and the levels of the conduction and valence bands are critical parameters in semiconductor photo-catalyst materials. For full water splitting, the CBM of monolayers and their corresponding heterostructures must be higher than the hydrogen reduction level (-4.44 eV), while the VBM must be below the oxygen oxidation level (-5.67 eV) [98]. The band levels of MoSSe/WSe_2, WSSe/WSe_2, and WSeTe/WSe_2 vdW heterostructures are shown in Figure 27.

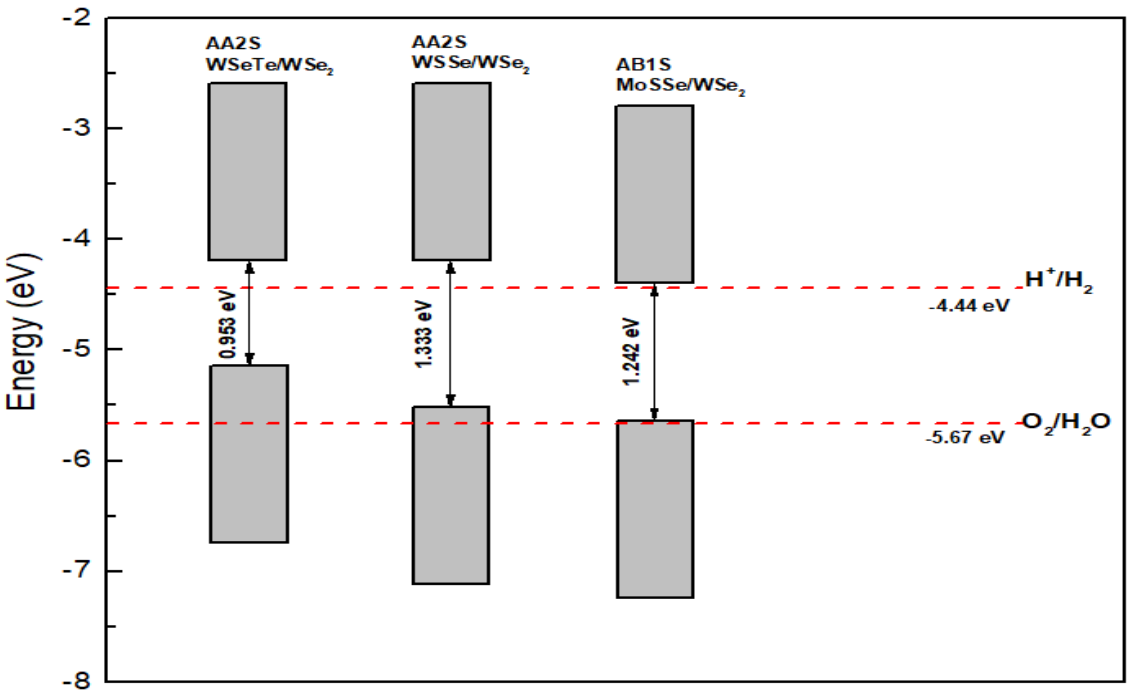

Figure 27. Relationship between Semiconductors Band Structure and Water Splitting Redox Potentials.

As shown in Figure 27, stable stacking of $MoSSe/WSe_2$, $WSSe/WSe_2$, and $WSeTe/WSe_2$, which, shows that not all these vdW heterostructures could well, satisfy the band edge requirements for full water splitting but good photo-catalyst for H_2 evolution under visible light irradiation.

Chapter 5 Conclusion and Future Work

5.1 Conclusion

In this work, we have developed the first principles DFT-based model to calculate electronic properties of $MoSSe/WSe_2$, $WSSe/WSe_2$, and $WSeTe/WSe_2$ vdW heterostructures for solar cell and photocatalytic water splitting applications.

In these heterostructures, eight different stacking modes were investigated to determine the most stable configuration based on binding energies and their variation with interlayer spacing. Out of eight stacking's three possible vdW heterostructures are the most stable configuration that are AB1S for $MoSSe/ WSe_2$, AA2S for $WSSe/ WSe_2$ and AA2S for $WSeTe/ WSe_2$. $MoSSe/ WSe_2$ and $WSeTe/ WSe_2$ are a direct bandgap material with band gap value of 1.2424 and 0.9527 eV, whereas $WSSe/ WSe_2$ is an indirect bandgap of 1.3331 eV. vdW heterostructures of different stacking orders show different gap nature depending on the strength of interlayer coupling. The type II band alignment in these heterostructures has been confirmed from the electronic band structures. The binding energy of $MoSSe/WSe_2$, $WSSe/WSe_2$, and $WSeTe/WSe_2$ heterostructures are found to be -18216.75 eV, -38995.69 eV, and -0.3296 eV at an interlayer layer distance of 5.75 Å, 4.05 Å, and 4.76 Å respectively. The photocatalytic properties of these vdW heterostructures in terms of band edge alignment have been studied as a function of pH =0-7. This reveals that not all of these heterostructures can satisfy the band edge requirements for full water splitting however can be applied for H_2 evolution reaction under visible light irradiation.

Type-II $MoSSe/WSe_2$, $WSSe/WSe_2$, and $WSeTe/WSe_2$ heterostructures have a great visible light absorption and they exhibit high solar PCE at the level of 20.16%, 20.48%, and 19.05%. The results demonstrate that these two 2D materials have great potential in the application of PV CSs based on van der Waals heterostructure.

5.2 Future work

DFT based electronic properties of $MoSSe/WSe_2$, $WSSe/WSe_2$, and $WSeTe/WSe_2$ vdW heterostructures for energy applications were investigated in this work. In the future, the heterostructures can be studied using the (HSE06) hybrid functional approximation to obtain better electronic properties. Because PBE underestimates the band gap, a computationally demanding hybrid functional (HSE06) is used to calculate the band edges and bandgap more accurately.

For further study, the following points are recommended:

- Investigate the remaining seven stacking modes for SC and full water splitting applications.
- The additional calculation will require, which are strain and electric field to make the heterostructures suitable for full water splitting.

References

[1] A. Holt and I. J. Pengelly, "ITS and renewable energy," *15th World Congr. Intell. Transp. Syst. ITS Am. Annu. Meet. 2008*, vol. 6, pp. 3854–3862, 2008, doi: 10.1049/ic.2008.0789.

[2] I. R. E. Agency, *Renewable Power Generation Costs in 2019*. 2020.

[3] A. Rawat, R. Ahammed, Dimple, N. Jena, M. K. Mohanta, and A. De Sarkar, "Solar Energy Harvesting in Type II van der Waals Heterostructures of Semiconducting Group III Monochalcogenide Monolayers," *J. Phys. Chem. C*, vol. 123, no. 20, pp. 12666–12675, 2019, doi: 10.1021/acs.jpcc.9b03359.

[4] T. Takata, C. Pan, and K. Domen, "Recent progress in oxynitride photocatalysts for visible-light-driven water splitting," *Sci. Technol. Adv. Mater.*, vol. 16, no. 3, 2015, doi: 10.1088/1468-6996/16/3/033506.

[5] K. Khan *et al.*, *Recent advances in two-dimensional materials and their nanocomposites in sustainable energy conversion applications*, vol. 11, no. 45. Royal Society of Chemistry, 2019.

[6] A. Kuc, *Two-dimensional transition-metal dichalcogenides Synthesis, Properties, and Applications*, vol. 11. 2015.

[7] K. S. Novoselov, A. Mishchenko, A. Carvalho, and A. H. Castro Neto, "2D materials and van der Waals heterostructures," *Science (80-.).*, vol. 353, no. 6298, 2016, doi: 10.1126/science.aac9439.

[8] W. Shi and Z. Wang, "Mechanical and electronic properties of Janus monolayer transition metal dichalcogenides," *J. Phys. Condens. Matter*, vol. 30, no. 21, May 2018, doi: 10.1088/1361-648X/aabd59.

[9] M. Chhowalla, H. S. Shin, G. Eda, L. J. Li, K. P. Loh, and H. Zhang, "The chemistry of two-dimensional layered transition metal dichalcogenide nanosheets," *Nature Chemistry*, vol. 5, no. 4. pp. 263–275, Apr. 2013, doi: 10.1038/nchem.1589.

[10] M. Chhowalla, Z. Liu, and H. Zhang, "Two-dimensional transition metal dichalcogenide (TMD) nanosheets," *Chemical Society Reviews*, vol. 44, no. 9. Royal Society of Chemistry, pp. 2584–2586, May 07, 2015, doi: 10.1039/c5cs90037a.

[11] E. Singh, K. S. Kim, G. Y. Yeom, and H. S. Nalwa, "Two-dimensional transition metal dichalcogenide-based counter electrodes for dye-sensitized solar cells," *RSC Advances*, vol. 7, no. 45. Royal Society of Chemistry, pp. 28234–28290, 2017, doi: 10.1039/c7ra03599c.

[12] D. Voiry, A. Mohite, and M. Chhowalla, "Phase engineering of transition metal dichalcogenides," *Chemical Society Reviews*, vol. 44, no. 9. Royal Society of Chemistry, pp. 2702–2712, May 07, 2015, doi: 10.1039/c5cs00151j.

[13] T. Akama, W. Okita, R. Nagai, C. Li, T. Kaneko, and T. Kato, "Schottky solar cell using few-layered transition metal dichalcogenides toward large-scale fabrication of semitransparent and flexible power generator," *Sci. Rep.*, vol. 7, no. 1, Dec. 2017, doi: 10.1038/s41598-017-12287-6.

[14] F. Li, W. Wei, P. Zhao, B. Huang, and Y. Dai, “Electronic and Optical Properties of Pristine and Vertical and Lateral Heterostructures of Janus MoSSe and WSSe,” *J. Phys. Chem. Lett.*, vol. 8, no. 23, pp. 5959–5965, Dec. 2017, doi: 10.1021/acs.jpclett.7b02841.

[15] Y. Yang *et al.*, “Structural and electronic properties of 2H phase Janus transition metal dichalcogenide bilayers,” *Superlattices Microstruct.*, vol. 131, pp. 8–14, 2019, doi: 10.1016/j.spmi.2019.05.027.

[16] M. Idrees *et al.*, “Electronic properties and enhanced photocatalytic performance of van der Waals heterostructures of ZnO and Janus transition metal dichalcogenides,” *Phys. Chem. Chem. Phys.*, vol. 22, no. 18, pp. 10351–10359, May 2020, doi: 10.1039/d0cp01264e.

[17] W. Chen, X. Hou, X. Shi, and H. Pan, “Two-Dimensional Janus Transition Metal Oxides and Chalcogenides: Multifunctional Properties for Photocatalysts, Electronics, and Energy Conversion,” *ACS Appl. Mater. Interfaces*, vol. 10, no. 41, pp. 35289–35295, 2018, doi: 10.1021/acsami.8b13248.

[18] M. Yagmurcukardes *et al.*, “Quantum properties and applications of 2D Janus crystals and their superlattices,” *Applied Physics Reviews*, vol. 7, no. 1. 2020, doi: 10.1063/1.5135306.

[19] L. Cao, Y. S. Ang, Q. Wu, and L. K. Ang, “Janus PtSSe and graphene heterostructure with tunable Schottky barrier,” *Appl. Phys. Lett.*, vol. 115, no. 24, Dec. 2019, doi: 10.1063/1.5130756.

[20] H. Schmidt, F. Giustiniano, and G. Eda, “Electronic transport properties of transition metal dichalcogenide field-effect devices: surface and interface effects,” *Chemical Society Reviews*, vol. 44, no. 21. Royal Society of Chemistry, pp. 7715–7736, Nov. 07, 2015, doi: 10.1039/c5cs00275c.

[21] R. C. on E. Pollution, *Novel Materials in the Environment : The case of nanotechnology Novel Materials in the Environment : The case of nanotechnology*, vol. 12, no. November. 2008.

[22] M. Z. Iqbal, S. Alam, M. M. Faisal, and S. Khan, “Recent advancement in the performance of solar cells by incorporating transition metal dichalcogenides as counter electrode and photoabsorber,” *Int. J. Energy Res.*, vol. 43, no. 8, pp. 3058–3079, 2019, doi: 10.1002/er.4375.

[23] N. Balis, E. Stratakis, and E. Kymakis, “Graphene and transition metal dichalcogenide nanosheets as charge transport layers for solution processed solar cells,” *Mater. Today*, vol. 19, no. 10, pp. 580–594, 2016, doi: 10.1016/j.mattod.2016.03.018.

[24] J. A. Luceño-Sánchez, A. M. Díez-Pascual, and R. P. Capilla, “Materials for photovoltaics: State of art and recent developments,” *Int. J. Mol. Sci.*, vol. 20, no. 4, 2019, doi: 10.3390/ijms20040976.

[25] K. Ranabhat, L. Patrikeev, A. A. evna Revina, K. Andrianov, V. Lapshinsky, and E. Sofronova, “An introduction to solar cell technology,” *J. Appl. Eng. Sci.*, vol. 14, no. 4, pp. 481–491, 2016, doi: 10.5937/jaes14-10879.

[26] S. Sharma, K. K. Jain, and A. Sharma, “Solar Cells: In Research and Applications—A

Review," *Mater. Sci. Appl.*, vol. 06, no. 12, pp. 1145–1155, 2015, doi: 10.4236/msa.2015.612113.

[27] M. A. Green *et al.*, "Solar cell efficiency tables (version 50)," *Prog. Photovoltaics Res. Appl.*, vol. 25, no. 7, pp. 668–676, 2017, doi: 10.1002/pip.2909.

[28] K. L. Chopra, P. D. Paulson, and V. Dutta, "Thin-film solar cells: An overview," *Prog. Photovoltaics Res. Appl.*, vol. 12, no. 2–3, pp. 69–92, 2004, doi: 10.1002/pip.541.

[29] M. GREEN *et al.*, "Solar cell efficiency tables (version 40)," *Ieee Trans Fuzzy Syst*, vol. 20, no. 6, pp. 1114–1129, 2012, doi: 10.1002/pip.

[30] S. Niki *et al.*, "CIGS absorbers and processes," *Prog. Photovoltaics Res. Appl.*, vol. 18, no. 6, pp. 453–466, 2010, doi: 10.1002/pip.969.

[31] S. Arul and R. Arun Kumar, "Synthesis and characterization of CuIn0.7Ga0.3Se2 (CIGS) bulk compound and hot wall deposited thin film absorber layer for solar cell applications," *Rasayan J. Chem.*, vol. 9, no. 2, pp. 278–286, 2016.

[32] J. Gong, J. Liang, and K. Sumathy, "Review on dye-sensitized solar cells (DSSCs): Fundamental concepts and novel materials," *Renew. Sustain. Energy Rev.*, vol. 16, no. 8, pp. 5848–5860, 2012, doi: 10.1016/j.rser.2012.04.044.

[33] Anders Hagfeldt and Michael Gratzel, "Hagfeldt, Grätzel - 2000 - Molecular Photovoltaics - Accounts of Chemical Research.pdf - Unknown.pdf - Unknown.pdf," *Acc. Chem. Res.*, vol. 33, no. 5, pp. 269–277, 2000.

[34] D. Bera, L. Qian, T. K. Tseng, and P. H. Holloway, "Quantum dots and their multimodal applications: A review," *Materials (Basel).*, vol. 3, no. 4, pp. 2260–2345, 2010, doi: 10.3390/ma3042260.

[35] J. Tian and G. Cao, "Semiconductor quantum dot-sensitized solar cells," *Nano Rev.*, vol. 4, no. 1, p. 22578, 2013, doi: 10.3402/nano.v4i0.22578.

[36] S. Almosni *et al.*, "Material challenges for solar cells in the twenty-first century: directions in emerging technologies," *Sci. Technol. Adv. Mater.*, vol. 19, no. 1, pp. 336–369, 2018, doi: 10.1080/14686996.2018.1433439.

[37] I. J. Kramer *et al.*, "Ordered nanopillar structured electrodes for depleted bulk heterojunction colloidal quantum dot solar cells," *Adv. Mater.*, vol. 24, no. 17, pp. 2315–2319, 2012, doi: 10.1002/adma.201104832.

[38] G. Giorgi, J. I. Fujisawa, H. Segawa, and K. Yamashita, "Small photocarrier effective masses featuring ambipolar transport in methylammonium lead iodide perovskite: A density functional analysis," *J. Phys. Chem. Lett.*, vol. 4, no. 24, pp. 4213–4216, 2013, doi: 10.1021/jz4023865.

[39] J. Jean *et al.*, "ZnO nanowire arrays for enhanced photocurrent in PbS quantum dot solar cells," *Adv. Mater.*, vol. 25, no. 20, pp. 2790–2796, 2013, doi: 10.1002/adma.201204192.

[40] H. Wang, T. Kubo, J. Nakazaki, T. Kinoshita, and H. Segawa, "PbS-quantum-dot-based heterojunction solar cells utilizing ZnO nanowires for high external quantum efficiency in

the near-infrared region," *J. Phys. Chem. Lett.*, vol. 4, no. 15, pp. 2455–2460, 2013, doi: 10.1021/jz4012299.

[41] Z. Yang *et al.*, "Colloidal Quantum Dot Photovoltaics Enhanced by Perovskite Shelling," *Nano Lett.*, vol. 15, no. 11, pp. 7539–7543, 2015, doi: 10.1021/acs.nanolett.5b03271.

[42] B. Hou *et al.*, "Highly Monodispersed PbS Quantum Dots for Outstanding Cascaded-Junction Solar Cells," *ACS Energy Lett.*, vol. 1, no. 4, pp. 834–839, 2016, doi: 10.1021/acsenergylett.6b00294.

[43] T. Y. Kim *et al.*, "Poly(3,4-ethylenedioxythiophene) Quantum Dot-Sensitized Solar Cells in the Solid-State Utilizing Polymer Electrolyte," *ACS Appl. Energy Mater.*, vol. 1, no. 2, pp. 290–295, 2018, doi: 10.1021/acsaem.7b00218.

[44] T. Sogabe, Q. Shen, and K. Yamaguchi, "Recent progress on quantum dot solar cells: a review," *J. Photonics Energy*, vol. 6, no. 4, p. 040901, 2016, doi: 10.1117/1.jpe.6.040901.

[45] H. Gaspar, F. Figueira, L. Pereira, A. Mendes, J. C. Viana, and G. Bernardo, "Recent developments in the optimization of the bulk heterojunction morphology of polymer: Fullerene solar cells," *Materials (Basel).*, vol. 11, no. 12, 2018, doi: 10.3390/ma11122560.

[46] D. Bryant *et al.*, "Light and oxygen induced degradation limits the operational stability of methylammonium lead triiodide perovskite solar cells," *Energy Environ. Sci.*, vol. 9, no. 5, pp. 1655–1660, 2016, doi: 10.1039/c6ee00409a.

[47] E. J. Juarez-Perez, L. K. Ono, M. Maeda, Y. Jiang, Z. Hawash, and Y. Qi, "Photodecomposition and thermal decomposition in methylammonium halide lead perovskites and inferred design principles to increase photovoltaic device stability," *J. Mater. Chem. A*, vol. 6, no. 20, pp. 9604–9612, 2018, doi: 10.1039/c8ta03501f.

[48] E. J. Juarez-Perez, Z. Hawash, S. R. Raga, L. K. Ono, and Y. Qi, "Thermal degradation of CH3NH3PbI3 perovskite into NH3 and CH3I gases observed by coupled thermogravimetry-mass spectrometry analysis," *Energy Environ. Sci.*, vol. 9, no. 11, pp. 3406–3410, 2016, doi: 10.1039/c6ee02016j.

[49] E. L. Unger *et al.*, "Hysteresis and transient behavior in current-voltage measurements of hybrid-perovskite absorber solar cells," *Energy Environ. Sci.*, vol. 7, no. 11, pp. 3690–3698, 2014, doi: 10.1039/c4ee02465f.

[50] K. A, T. K, S. Y, and M. T, "Organometal halide perovskites as visible-light sensitizers for photovoltaic cells," *J. Am. Chem. Soc.*, vol. 131, no. 17, pp. 6050–1, 2009.

[51] A. B. Djurišić *et al.*, "Perovskite solar cells - An overview of critical issues," *Prog. Quantum Electron.*, vol. 53, no. June, pp. 1–37, 2017, doi: 10.1016/j.pquantelec.2017.05.002.

[52] B. Salhi, Y. S. Wudil, M. K. Hossain, A. Al-Ahmed, and F. A. Al-Sulaiman, "Review of recent developments and persistent challenges in stability of perovskite solar cells," *Renew. Sustain. Energy Rev.*, vol. 90, no. March, pp. 210–222, 2018, doi: 10.1016/j.rser.2018.03.058.

[53] R. Z. Tala-ighil, “Handbook of Nanoelectrochemistry,” *Handb. Nanoelectrochemistry*, no. October, 2016, doi: 10.1007/978-3-319-15207-3.

[54] K. D. G. I. Jayawardena, L. J. Rozanski, C. A. Mills, M. J. Beliatis, N. A. Nismy, and S. R. P. Silva, “‘Inorganics-in-Organics’: Recent developments and outlook for 4G polymer solar cells,” *Nanoscale*, vol. 5, no. 18, pp. 8411–8427, 2013, doi: 10.1039/c3nr02733c.

[55] P. G. V. Sampaio and M. O. A. González, “Photovoltaic solar energy: Conceptual framework,” *Renew. Sustain. Energy Rev.*, vol. 74, no. December 2016, pp. 590–601, 2017, doi: 10.1016/j.rser.2017.02.081.

[56] M. Kivambe, B. Aissa, and N. Tabet, “Emerging Technologies in Crystal Growth of Photovoltaic Silicon: Progress and Challenges,” *Energy Procedia*, vol. 130, pp. 7–13, 2017, doi: 10.1016/j.egypro.2017.09.405.

[57] B. S. Xakalashe and M. Tangstad, “Silicon processing: from quartz to crystalline silicon solar cells,” *South. African Pyromethallurgy Int. Conf.*, no. March, pp. 1–18, 2011.

[58] J. Grandidier, D. M. Callahan, J. N. Munday, and H. a Atwater, “Enhancement Using Whispering Gallery Modes of Dielectric Nanospheres,” *Ieee J. Photovoltaics*, vol. 2, no. 2, pp. 123–128, 2012.

[59] B. Hemavathi, T. N. Ahipa, and R. K. Pai, “Polymer design for solar cell - Current trend and future scenario,” *Eur. Polym. J.*, vol. 72, pp. 309–340, 2015, doi: 10.1016/j.eurpolymj.2015.09.017.

[60] N. Marinova, S. Valero, and J. L. Delgado, “Organic and perovskite solar cells: Working principles, materials and interfaces,” *J. Colloid Interface Sci.*, vol. 488, pp. 373–389, 2017, doi: 10.1016/j.jcis.2016.11.021.

[61] S. P. Philipps and A. W. Bett, “III-V Multi-junction solar cells and concentrating photovoltaic (CPV) systems,” *Adv. Opt. Technol.*, vol. 3, no. 5–6, pp. 469–478, 2014, doi: 10.1515/aot-2014-0051.

[62] M. Yamaguchi, “Japanese R&D activities of high efficiency III-V compound multi-junction and concentrator solar cells,” *Energy Procedia*, vol. 15, no. 2011, pp. 265–274, 2012, doi: 10.1016/j.egypro.2012.02.031.

[63] J. M. Lee, J. S. Park, S. H. Lee, H. Kim, S. Yoo, and S. O. Kim, “Selective electron- or hole-transport enhancement in bulk-heterojunction organic solar cells with N- or B-doped carbon nanotubes,” *Adv. Mater.*, vol. 23, no. 5, pp. 629–633, 2011, doi: 10.1002/adma.201003296.

[64] Z. Ma *et al.*, “InSe/Te van derWaals Heterostructure as a High-Efficiency Solar Cell from Computational Screening,” *Materials (Basel).*, vol. 14, 2021, doi: https://doi.org/10.3390/ma14143768.

[65] V. M. Andreev, “SEMICONDUCTOR HETEROSTRUCTURES Heterostructure solar cells,” *Semiconductors*, vol. 33, no. 9, pp. 9–12, 1999.

[66] P. Lin and J. Yang, “Tunable WSe2/WS2 van der Waals heterojunction for self-powered photodetector and photovoltaics,” *J. Alloys Compd.*, vol. 842, p. 155890, 2020, doi:

10.1016/j.jallcom.2020.155890.

[67] X. Zheng *et al.*, “PN/PAs-WSe2 van der Waals heterostructures for solar cell and photodetector,” *Sci. Rep.*, vol. 10, no. 1, pp. 1–9, 2020, doi: 10.1038/s41598-020-73152-7.

[68] J. Chen *et al.*, “III-VI van der Waals heterostructures for sustainable energy related applications,” *Nanoscale*, vol. 11, no. 13, pp. 6431–6444, 2019, doi: 10.1039/C9NR00421A.

[69] D. Nutting *et al.*, “Heterostructures formed through abraded van der Waals materials,” *Nat. Commun.*, vol. 11, no. 1, pp. 1–10, 2020, doi: 10.1038/s41467-020-16717-4.

[70] Y. Jing, B. Liu, X. Zhu, F. Ouyang, J. Sun, and Y. Zhou, “Tunable electronic structure of two-dimensional transition metal chalcogenides for optoelectronic applications,” *Nanophotonics*, vol. 9, no. 7. De Gruyter, pp. 1675–1694, Jul. 01, 2020, doi: 10.1515/nanoph-2019-0574.

[71] H. Taghinejad, A. A. Eftekhar, and A. Adibi, “Lateral and vertical heterostructures in two-dimensional transition-metal dichalcogenides [Invited],” *Opt. Mater. Express*, vol. 9, no. 4, p. 1590, Apr. 2019, doi: 10.1364/ome.9.001590.

[72] M. Idrees *et al.*, “Optoelectronic and solar cell applications of Janus monolayers and their van der Waals heterostructures,” *Phys. Chem. Chem. Phys.*, vol. 21, no. 34, pp. 18612–18621, Aug. 2019, doi: 10.1039/c9cp02648g.

[73] A. Kudo and Y. Miseki, “Heterogeneous photocatalyst materials for water splitting,” *Chem. Soc. Rev.*, vol. 38, no. 1, pp. 253–278, 2009, doi: 10.1039/b800489g.

[74] B. Y. Alfaifi, H. Ullah, S. Alfaifi, A. A. Tahir, and T. K. Mallick, “Photoelectrochemical solar water splitting: From basic principles to advanced devices,” *Veruscript Funct. Nanomater.*, vol. 2, no. February, p. BDJOC3, 2018, doi: 10.22261/fnan.bdjoc3.

[75] X. Chen, S. Shen, L. Guo, and S. S. Mao, “Semiconductor-based photocatalytic hydrogen generation,” *Chem. Rev.*, vol. 110, no. 11, pp. 6503–6570, 2010, doi: 10.1021/cr1001645.

[76] R. Li, “Latest progress in hydrogen production from solar water splitting via photocatalysis, photoelectrochemical, and photovoltaic-photoelectrochemical solutions,” *Cuihua Xuebao/Chinese J. Catal.*, vol. 38, no. 1, pp. 5–12, 2017, doi: 10.1016/S1872-2067(16)62552-4.

[77] R. Abe, “Recent progress on photocatalytic and photoelectrochemical water splitting under visible light irradiation,” *J. Photochem. Photobiol. C Photochem. Rev.*, vol. 11, no. 4, pp. 179–209, 2010, doi: 10.1016/j.jphotochemrev.2011.02.003.

[78] B. M. Hunter, H. B. Gray, and A. M. Müller, “Earth-Abundant Heterogeneous Water Oxidation Catalysts,” *Chem. Rev.*, vol. 116, no. 22, pp. 14120–14136, 2016, doi: 10.1021/acs.chemrev.6b00398.

[79] K. Capelle, “A bird’s-eye view of density-functional theory,” *Brazilian J. Phys.*, vol. 36, no. 4 A, pp. 1318–1341, 2006, doi: 10.1590/s0103-97332006000700035.

[80] E. R. Homer, L. Li, and C. A. Schuh, “Kinetic monte carlo modeling of nanomechanics in

amorphous systems," *Springer Ser. Mater. Sci.*, vol. 245, pp. 441–468, 2016, doi: 10.1007/978-3-319-33480-6.

[81] J. VOSS, "Exchange-correlation Functionals," *stanford*, 2021. http://stanford.edu/~vossj/slac/project/xc-functionals/.

[82] S. Chretien, S. Barbara, and D. R. Salahub, *Atomic clusters and nanoparticles. Agregats atomiques et nanoparticules*, no. May 2014. 2001.

[83] Q. ESPRESSO, "General documentation," *QEF MAX*, 2019. https://www.quantum-espresso.org/resources/users-manual.

[84] M. Boero and A. Oshiyama, "Encyclopedia of Nanotechnology," *Encycl. Nanotechnol.*, pp. 1–10, 2020, doi: 10.1007/978-94-007-6178-0.

[85] P.-K. Network, "Software codes," *psi-k*, 2021. https://psi-k.net/software/.

[86] M. Studio, "' Materials Studio 2016 ' 新功能发布 Materials Studio 2016 新功能亮点," *pan-data*, 2016. https://software.pan-data.eu/software/86/materials-studio.

[87] K. Momma and F. Ijumi, "VESTA Vizualization for Electronic and STructural Analyzis," 2016. https://jp-minerals.org/vesta/en/.

[88] L. E. Ratcliff, N. D. M. Hine, and P. D. Haynes, "Calculating optical absorption spectra for large systems using linear-scaling density functional theory," *Phys. Rev. B - Condens. Matter Mater. Phys.*, vol. 84, no. 16, pp. 18–20, 2011, doi: 10.1103/PhysRevB.84.165131.

[89] L.E. Toth, "Transition Metal Carbides and Multilayers," no. January 2010, p. 296, 1971.

[90] Materials Square, "Convergence Test: Cutoff Energy Optimization for Silicon Bulk," *Materials Square Tech Blog*, 2019. https://beta.materialssquare.com/blog/1-convergence-test-cutoff-energy-optimization-for-silicon-bulk%0Ahttps://blog.virtuallab.co.kr/en/2019/05/17/1-convergence-test-cutoff-energy-optimization-for-silicon-bulk/.

[91] L. Cao, Y. Deng, H. Gao, Y. Wang, X. Chen, and Z. Zhu, "Towards high refrigeration capability: The controllable structure of hierarchical Bi0.5Sb1.5Te3 flakes on a metal electrode," *Phys. Chem. Chem. Phys.*, vol. 17, no. 10, pp. 6809–6818, 2015, doi: 10.1039/c4cp05386a.

[92] S. Wang, H. Tian, C. Ren, J. Yu, and M. Sun, "Electronic and optical properties of heterostructures based on transition metal dichalcogenides and graphene-like zinc oxide," *Sci. Rep.*, no. July, pp. 6–11, 2018, doi: 10.1038/s41598-018-30614-3.

[93] Y. Zhang, R. Xiong, B. Sa, J. Zhou, and Z. Sun, "MXenes: Promising donor and acceptor materials for high-efficiency heterostructure solar cells," *Sustain. Energy Fuels*, vol. 5, no. 1, pp. 135–143, 2021, doi: 10.1039/d0se01443e.

[94] Q. Su *et al.*, "Heterojunction Photocatalysts Based on 2D Materials: The Role of Configuration," *Adv. Sustain. Syst.*, vol. 4, no. 9, pp. 1–19, 2020, doi: 10.1002/adsu.202000130.

[95] K. Langfeld, “Density of states,” *Proc. Sci.*, vol. Part F1285, pp. 1–7, 2016, doi: 10.1093/acprof:oso/9780199534937.003.0010.

[96] M. R. Filip, C. Verdi, and F. Giustino, “GW Band Structures and Carrier Effective Masses of CH3NH3PbI3 and Hypothetical Perovskites of the Type APbI3: A = NH4, PH4, AsH4, and SbH4,” *J. Phys. Chem. C*, vol. 119, no. 45, pp. 25209–25219, 2015, doi: 10.1021/acs.jpcc.5b07891.

[97] A. Rawat, M. K. Mohanta, N. Jena, Dimple, R. Ahammed, and A. De Sarkar, “Nanoscale Interfaces of Janus Monolayers of Transition Metal Dichalcogenides for 2D Photovoltaic and Piezoelectric Applications,” *J. Phys. Chem. C*, vol. 124, no. 19, pp. 10385–10397, 2020, doi: 10.1021/acs.jpcc.0c02199.

[98] M. Idrees *et al.*, “Optoelectronic and solar cell applications of Janus monolayers and their van der Waals heterostructures,” *Phys. Chem. Chem. Phys.*, vol. 21, no. 34, pp. 18612–18621, 2019, doi: 10.1039/c9cp02648g.